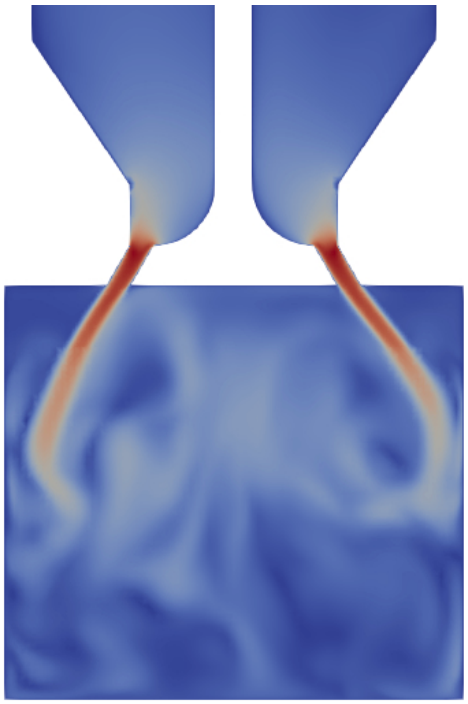

Performance comparison of simulation models and parameters for engine CFD applications

Master's thesis in Innovative Sustainable Energy Engineering

ILMARI OINONEN

DEPARTMENT OF MECHANICS AND MARITIME SCIENCES
CHALMERS UNIVERSITY OF TECHNOLOGY
Gothenburg, Sweden 2025
www.chalmers.se

Master's thesis 2025

Performance comparison of simulation models and parameters for engine CFD applications

ILMARI OINONEN

CHALMERS
UNIVERSITY OF TECHNOLOGY

Department of Mechanics and Maritime Sciences
Division of Fluid Dynamics
Chalmers University of Technology
Gothenburg, Sweden 2025

Performance comparison of simulation models and parameters for engine CFD applications
ILMARI OINONEN

Supervisors: D.Sc. Karri Keskinen & D.Sc. Bulut Tekgül, Wärtsilä Oyj Abp
Examiner: Prof. Håkan Nilsson, Department of Mechanics and Maritime Sciences

Master's Thesis 2025
Department of Mechanics and Maritime Sciences
Division of Fluid Dynamics
Chalmers University of Technology
SE-412 96 Gothenburg
Telephone +46 31 772 1000

Cover: Cut plane of the simulated velocity field inside the Imperial college engine model.

Typeset in LaTeX
Gothenburg, Sweden 2025

Performance comparison of simulation models and parameters for engine CFD applications
ILMARI OINONEN
Department of Mechanics and Maritime Sciences
Chalmers University of Technology

Abstract

In this thesis, the performance of computational fluid dynamics (CFD) simulation models and parameters are systematically compared for an engine model based on the Imperial college experimental engine. A set of simulation models and parameters were chosen to be studied. For each model and parameter, a few different options were chosen and simulation cases created for each possible different combination of these options. A custom code was written for creating the cases out of all the combinations of model and parameter options.

The simulations for this thesis were performed with OpenFOAM, which is an open-source CFD software. The engine model has been created at Wärtsilä and used in-house meshing tools to create a moving mesh.

After the simulations had ran, the results were post-processed using a custom code written for this thesis. The post-processed results were directly compared to results from a high-fidelity direct numerical simulation (DNS) study based on the Imperial college case, which has great agreement with the experimental results. For each simulation, two metrics were calculated that measured the difference between simulation and DNS results. These metrics were used to assess the performance differences between cases with different model and parameter combinations, and thus the performance of the models and parameters themselves.

The models and parameters studied in this thesis were the turbulence model, velocity advection scheme, maximum Courant number, mesh resolution and the number and thickness of surface inflation layers of the mesh. These were divided into three individual studies.

A few of the turbulence models had clearly better performance than the others. Change in the velocity advection scheme, maximum Courant number and surface inflation parameters had only slight effects on performance. An increased mesh resolution generally lead to better performance.

Keywords: Imperial college engine, CFD, OpenFOAM, Turbulence modelling, Meshing

Acknowledgements

I would like to thank Wärtsilä Oyj Abp for funding and providing resources for this thesis, and the Thermofluids & Simulations team for taking me under their wing and providing help and tools that have been essential for this thesis. Biggest thanks to Dr. Karri Keskinen and Dr. Bulut Tekgül for supervising my thesis and for their continuous support, guidance, expertise and mentorship. Thank you to Prof. Håkan Nilsson for examining my thesis. I would also like to thank my manager Mr. Éric Lendormy.

Ilmari Oinonen, Espoo, December 12, 2025

List of Acronyms

Below is the list of acronyms that have been used throughout this thesis listed in alphabetical order:

BC	Boundary condition
CFD	Computational fluid dynamics
DNS	Direct numerical simulation
DOE	Design of experiment
FVM	Finite volume method
IC	Initial condition
LES	Large eddy simulation
LSR	Length scale resolution
MAE	Mean absolute error
MSE	Mean square error
RANS	Reynolds-averaged Navier-Stokes
PBiCGStab	Preconditioned bi-conjugate gradient stabilized
PCG	Preconditioned conjugate gradient
PISO	Pressure-implicit with splitting of operators
rms	Root mean square
rpm	Revolutions per minute
SIMPLE	Semi-implicit method for pressure-linked equations
WALE	Wall-adapting local eddy-viscosity

Nomenclature

Below is the nomenclature of parameters that have been used throughout this thesis.

Parameters

$C_{\varepsilon 1}, C_{\varepsilon 2}$	Constants in the model equation for ε
$C_{\omega 1}, C_{\omega 2}$	Constants in the model equation for ω
Co	Courant number
$\mathbf{F}$	Flux
$G(r)$	Filter function
k	Turbulent kinetic energy
k_{mod}	Modelled turbulent kinetic energy
k_{res}	Resolved turbulent kinetic energy
L	(Characteristic) length
$\mathcal{P}$	Production rate of turbulent kinetic energy
p	Static pressure
$\langle p \rangle$	Mean static pressure
$\mathbf{Q_S}$	Surface source
Q_V	Internal source
Re	Reynolds number
$\mathbf{S}$	Surface
$\bar{S}_{ij}$	Mean rate-of-strain tensor
s_e	Engine stroke
t	Time
$\boldsymbol{U}$	Velocity
$\overline{U}$	Filtered velocity
$\langle \boldsymbol{U} \rangle$	Mean velocity
$\langle U \rangle_E$	Ensemble average of velocity

$U_{p,mean}$	Average piston velocity
$U_{rms,mod}$	Modelled root mean square of velocity
$U_{z,rms,mod}$	Modelled root mean square of axial velocity
$U_{z,rms,res}$	Resolved root mean square of axial velocity
$U_{z,rms,tot}$	Total root mean square of axial velocity
$\boldsymbol{u}$	Fluctuating velocity
u'	Residual velocity
u_η	Kolmogorov scale of velocity
x	Cartesian coordinate
β	Limiter
δ_{ij}	Kronecker delta
ε	Dissipation rate of turbulent kinetic energy
η	Kolmogorov scale of length
ν	Kinematic viscosity
ν_{eff}	Effective viscosity
ν_T	Turbulent viscosity
ρ	Density
σ_ε	Turbulent Prandtl number for dissipation
σ_k	Turbulent Prandtl number for kinetic energy
σ_ω	Turbulent Prandtl number for dissipation
τ_η	Kolmogorov scale of time
Ψ	Non-specified scalar property
$\boldsymbol{\Psi}$	Non-specified field property
Ω	Control volume
ω	Specific rate of dissipation of turbulent kinetic energy
ω_e	Engine angular velocity

Contents

1

Introduction

The internal combustion engine has been a staple for providing energy in the transportation industry now for over a century. Its popularity can be largely credited to the inherent scalability of its design, as the number and volume of its combustion chambers can be varied, both directly affecting the power output. Different iterations of the same engine design can be applied to a great variety of different solutions, ranging from smaller consumer motorboat and automotive engines, all the way to the engines of the largest marine vessels.

While the standard operating principle of the internal combustion engine has remained the same, the more intricate parts of its design and the development of parts and fuels have progressed throughout the years. Engine manufacturers are constantly trying to produce engines that are more fuel efficient, produce less emissions, less prone to malfunction, cheaper to manufacture, etc.

The process of engine development can take many forms. A traditional and reliable way is to create a prototype engine, run it and then gather data of its performance with different sensors. This data can then be compared to previous experiments and assessments of the prototype's performance can be made. While this kind of an experimental approach does produce results that are very accurate or even exact to the real performance of the engine, producing the prototypes themselves can be very expensive and getting good quality and high-resolution measurements can be difficult. Especially with flow phenomena, it can be difficult to get measurements of flow properties without disrupting the flow.

Another way to drive engine development is by modelling. With modelling, a virtual or otherwise non-physical model of the engine is created based on the known physics that can be applied for engines, such as fluid mechanics, thermodynamics and combustion chemistry.

The drawback to modelling is that it can never reach full agreement with reality as some details of the physics will always have to be omitted. It is up to the modeller to choose how accurate they want their model to be and what properties of the engine are they interested in. A more detailed model is generally also more expensive, be it with an increased requirement of computational resources or more effort from the modeller in defining the model.

Models often have several different places where approximations are made for the

sake of pure feasibility of the model or efficiency. Choosing the means of approximation for some physical phenomena is no simple task and there often are no absolute correct answers. Moreover, the differences between modelling approximations can be worth studying intrinsically.

1.1 Objective definition

The objective of the thesis is to investigate the performance differences of different computational fluid dynamics (CFD) modelling options and parameters for an engine case. There is a vast amount of different models for solving fluid flows, many of which work better in some situations than in others. When approaching a fluid flow modelling case, it isn't necessarily feasible to thoroughly consider each individual model or parameter choice, but rather rely on choices that have worked before and produced satisfying results. This thesis aims to bring more robustness to some of the model and parameter choices for engine modelling.

In order to gain validity for the study, the main point of comparison should be based in reality. Well-documented experimental studies have been performed of engines in operating conditions, such as the Imperial college engine [1], the TCC-III engine [2] and TU Darmstadt engine [3]. Measurements from such experiments should be used as the foundation for the benchmarking.

Experimental reference data is often much more sparse than data from CFD simulations and thus cannot act as a point of comparison when modelling for many flow properties of interest. One part of the thesis is to determine or calculate a low-dimensional quantity that can be extracted from each simulation case, which also represents well the accuracy of the simulation compared to reference data. This quantity could be a single number that is comparable to the magnitude of error that the simulation has compared to reference data. While concentrating the vast amount of data that comes from a CFD simulations to a singular number loses most of the information that is available, it makes it easier to effectively compare a larger set of simulations to each other.

2

Theoretical background

In order to create an engine model that is able to reliably produce useful results, one must base it on the relevant theory. The operation of an engine can be studied from the point of view of fluid mechanics, thermodynamics, material sciences, or structural analysis to name a few, and often many of these fields are considered simultaneously. Furthermore, the physics in question can also be studied to varying degrees of depth, ranging from the molecular level to a continuum assumption.

Increasing the accuracy and scope of a model generally comes with an increased demand for resources and creating a model that would perfectly mimic reality is not feasible with modern technology. It is the responsibility of the modeller to choose which physics to consider in their model and to what degree of precision.

In terms of physics, this thesis considers fluid mechanics and thermodynamics relevant to an engine under operating conditions. Additionally, since the subject of study is a computational model, computational sciences are also considered.

2.1 Finite volume method

When modelling a fluid flow with a computer, both the control volume and time have to be discretized instead of using a continuum model. Also, the partial differential equations that govern fluid flow, such as the Navier-Stokes equations, cannot be solved analytically for other than very simple flow geometries. Discretization divides the flow properties into a discrete set of points or cells in the control volume and time into discreet time steps.

The CFD simulations done for this thesis are run with the OpenFOAM developer version. In OpenFOAM, the volumetric discretization of the governing equations is done through the finite volume method (FVM). The strength of the FVM is based on the its direct discretization of the integral form of the conservation law. This is in contrast to the finite difference method which uses the differential forms of conservation laws. [4]

The conservation law states that a flow quantity inside a given control volume should vary equally to the sum of all fluxes in and out of the volume and the sources and sinks inside the volume of that quantity. If this is true, there should be no unexplainable gains or losses of the quantity. Mathematically, the integral form of the

conservation law is

$$\frac{\partial \Psi}{\partial t}_{\Omega} = \int_{\Omega} Q_V d\Omega - \oint_S \boldsymbol{F} \cdot d\boldsymbol{S} + \oint_S \boldsymbol{Q_S} \cdot d\boldsymbol{S}, \tag{2.1}$$

where the time development of flow quantity Ψ inside the control volume Ω is equal to the sum of internal sources Q_V, and fluxes $\mathbf{F}$ and surface sources $\mathbf{Q_S}$ through the control volume surface $\mathbf{S}$ [4].

The FVM takes the control volume of the flow case of interest and divides it into multiple smaller control volumes. The conservation law would be difficult or impossible to solve analytically for the original control volume, due to complex geometries that would make the integrals of the conservation law equation unsolvable, for example. Also, the distribution of flow quantities inside the original control volume is usually complex, so that they cannot be stated analytically. The smaller control volumes, that the original control volume is divided into, are generally very simple in their geometry, such as hexahedra for three dimensional cases or quadrilaterals for two dimensional cases. Calculating the integrals for these kind of shapes is trivial, and they also work as discrete stations at which flow quantities can be evaluated with a single value or vector, at a specific point of the control volume. The latter partially solves the problem of defining the complex fields of flow quantities, but creates a new problem where the flow quantities are explicitly defined only at the volumetric resolution of the discretization, which introduces discretization error.

2.2 Meshing

The grid of points and control volumes that is produced by volumetric discretization is commonly known as a mesh. In OpenFOAM, the FVM mesh is made up of polyhedral cells that equate to the control volumes that the flow case volume is discretized into. Each cell is completely surrounded by other cells or by the boundaries of the geometry. The boundaries of the cells are called faces and are shared between adjacent cells. The flow property values for each cell are located in the center of the cell and for each face in the center of the face. The schematic of a cell is illustrated in figure 2.1.

The dimensions of the mesh define the volumetric resolution of the model. Larger cell sizes mean that field values are distributed more sparsely for a given volume and that the values on cell faces have to be interpolated over larger distances. This in turn produces a larger interpolation error. Larger cell sizes almost always correspond to worse accuracy due to the larger interpolation error, but this correspondence is not independent of other factors.

Smaller cell sizes lead to an increased amount of cells and a larger cell count requires more computational resources as the field values for each cell will have to be solved. Meshing therefore becomes a compromise between accuracy and computational affordability. It is often beneficial to have different cell sizes in different parts of the mesh. When field gradients are large and thus also the differences of values

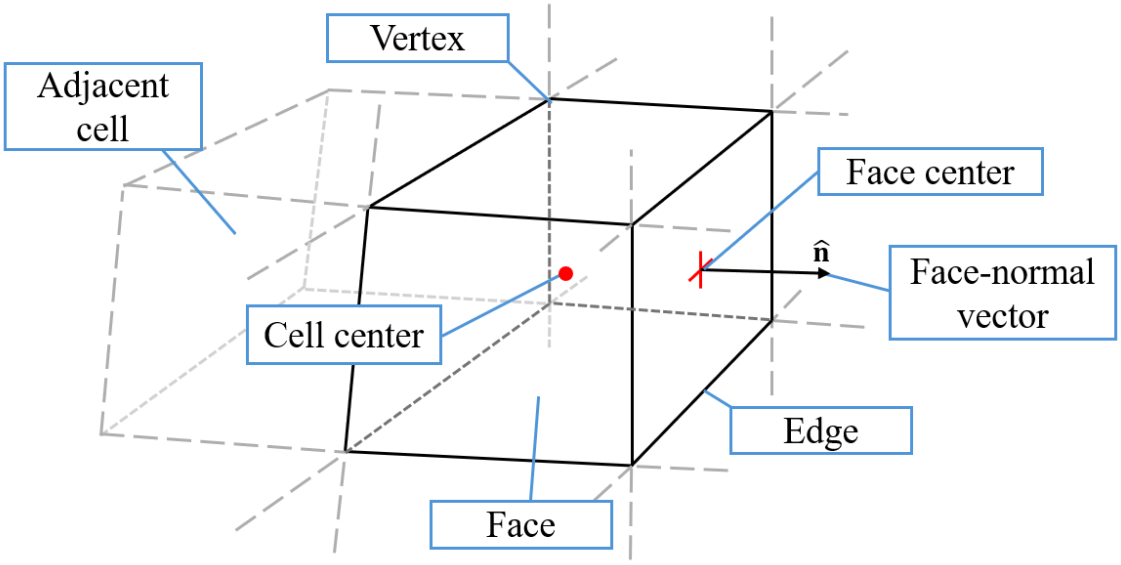

Figure 2.1: A hexahedral cell from a three-dimensional structured non-Cartesian mesh.

for points that are used for interpolation, the interpolation error increases relative to the difference. In these situations smaller cell sizes should be employed to reduce the value difference. In turn for locations of lesser gradients, the cell sizes have less effect on the interpolation error and thus larger cell sizes can be used without a large negative impact on the accuracy of the overall solution. A common way of defining a mesh is by assigning the largest desirable cell size as a base cell size and then defining refinement zones where the cell sizes are a portion of the base cell size.

A special case of refinement are inflation layers. They are used for locations where boundary layers are formed, such as solid walls. Inflation layer cells have a significantly reduced size in the direction normal to the surface, as the field gradients caused by the boundary layer are also large in that direction.

Structured and unstructured meshes

Meshes can be divided into structured and unstructured meshes. Structured meshes are quadrilateral for two-dimensional and hexahedral for three-dimensional cases, and arranged in a Cartesian or curvilinear structure. Unstructured meshes can be formed of any kind of polygons for two-dimensional or polyhedra for three-dimensional cases. [5]

Unstructured and non-Cartesian structured meshes can fall victim to additional sources of error. This is due to the center of a face between two cells possibly not aligning with a line drawn between the centers of the cells [5]. In such cases, by choosing to represent the face center as the intersection between the face and the cell center line, or by extrapolating from the intersection point to the face center, error is produced in either case. Structured Cartesian meshes do not have this problem,

which makes using one generally more desirable.

2.3 Numerical schemes

The governing partial differential equations of fluid flow are analytically solvable only for very simple geometries. The FVM is used to divide flow cases into a collection of smaller and simpler control volumes, but even in that case, the resulting geometries usually aren't simple enough for solving the governing equations analytically. The FVM control volumes are, however, simple enough in geometry that numerical schemes can be applied to simplify, or discretize the equations.

An essential mathematical property for discretizing the governing equations is Gauss's theorem which states that

$$\int_{\Omega} \nabla \cdot \boldsymbol{\Psi} d\Omega = \oint_{S} \boldsymbol{\Psi} \cdot d\boldsymbol{S}. \tag{2.2}$$

It means that the collective divergence of a field $\boldsymbol{\Psi}$ inside a control volume Ω is equal to the flux of field $\boldsymbol{\Psi}$ through the surface S of the control volume. Terms including divergence calculations are very common in the governing equations of fluid flow. Gauss's theorem allows for these terms to be determined without the knowledge of the complete flow field inside control volumes, but rather the fluxes in and out of them. This is very useful in terms of the FVM, as inside the small control volumes, the complete flow field is unknown.

Like all means of approximation, numerical schemes produce error. In their case, the errors can be divided into two main categories, dispersion and diffusion. Numerical dispersion causes solutions to be unstable and larger variations in the solution than what is expected in the phenomenon that is being modelled as presented on the left side of figure 2.2. Numerical diffusion doesn't cause instability, but instead causes the solution to smear out towards uniformity and with decreasing accuracy as presented on the right side of figure 2.2. The linear interpolation scheme is per-

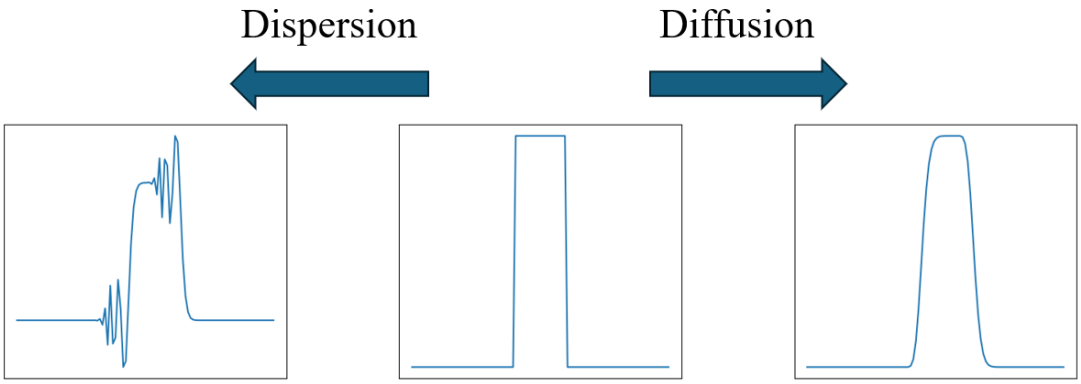

Figure 2.2: Effects of numerical dispersion and diffusion on a pulse.

haps the conceptually simplest numerical scheme. To approximate a field value on

a control volume face using the linear interpolation scheme, a weighted average of values at the cell-centers of control volumes that share the face is taken, based on the respective distances to the face. The value for field Ψ at the face would be

$$\Psi_f = d\Psi_A + (1-d)\Psi_B, \tag{2.3}$$

where $d = |\boldsymbol{F} - \boldsymbol{A}|/|\boldsymbol{B} - \boldsymbol{A}|$ and $\boldsymbol{A}$,$\boldsymbol{B}$ are the locations for the cell-centers and $\boldsymbol{F}$ for the intersection of the face and a line between the cell-centers. The linear interpolation scheme is dispersive by nature.

Another well-known numerical scheme in fluid flow modelling is the upwind scheme. In the upwind scheme, the gradient of a field $\partial\Psi/\partial x$ at a cell center is calculated between the cell in question and the cell upwind, so the cell that is on the opposite direction of the flow direction. The upwind scheme is sensible for flow cases, as flow properties are often carried to the direction of the flow. The upwind scheme is very diffusive by nature.

There are many more numerical schemes that are used for fluid flow modelling. They are often combinations of the linear interpolation and upwind schemes, having also a mixture of the strengths and weaknesses of both schemes. A typical method of doing this is by combining the schemes with an addition of a limiter

$$\Psi_f = (1-\beta)\Psi_U + \beta\Psi_L. \tag{2.4}$$

The value of the limiter defines the behavior of the scheme. For example, with $\beta = 0$ the scheme behaves as the upwind scheme and with $\beta = 1$ it behaves as the linear scheme. With $\beta = 2$ the scheme behaves as the downwind scheme, which is similar to the upwind scheme except, as per the name, the gradient $\partial\Psi/\partial x$ is calculated using the cell downwind, instead of upwind. Schemes using a limiter are called limited schemes, and they often include also a method of calculating β for each cell face. [6]

2.4 Temporal discretization

The time dependent nature of flow phenomena is housed in the time derivative term $\frac{\partial\Psi}{\partial t}$ in the governing equations. The equations have to be discretized also temporally since solving them continuously in time isn't possible. This is done through the definition of a time step Δt. The time step can be constant, but often it is set to depend on other factors. The governing equations are solved repeatedly by incrementing time with the amount of the time step, starting from an initial condition of the flow field. The time derivative term is discretized using a numerical scheme. The simplest time discretization scheme is the Euler scheme

$$\frac{\partial\Psi}{\partial t} \rightarrow \frac{\Psi^{t_2} - \Psi^{t_1}}{\Delta t} \tag{2.5}$$

which approximates the time derivative as a difference between states of the flow field one time step apart, divided by the length of the time step [6]. Applying this

to the conservation law (2.1) would give

$$\Psi^{t_2} = \Psi^{t_1} + \Delta t \left(\int_\Omega Q_V^{t_1} d\Omega - \oint_S \boldsymbol{F}^{t_1} \cdot d\boldsymbol{S} + \oint_S \boldsymbol{Q}_S^{t_1} \cdot d\boldsymbol{S} \right), \tag{2.6}$$

where all the right side terms would in this case be known, as they are based on the current time instance t_1, making it possible to calculate the flow field for the next time instance t_2. A time discretization scheme which allows the next time instance to be calculated purely based on the current one, is called explicit. Explicit schemes are simple to implement, but have stability issues.

The FVM typically uses implicit schemes instead of explicit. Implicit schemes are more stable, but their formulation includes terms from the same time instance that is being solved, like for the backward scheme

$$\frac{\partial \Psi}{\partial t} \rightarrow \frac{3\Psi^{t_3} - 4\Psi^{t_2} + \Psi^{t_1}}{2\Delta t}. \tag{2.7}$$

This means that the solution has to be calculated for all cells simultaneously, unlike explicit schemes, where each cell can be solved individually.

2.4.1 Courant-Friedrichs-Lewy condition

The Courant-Friedrichs-Lewy (CFL) condition is a condition for the length of the time step that has to be fulfilled in order to ensure convergence. The condition is that the Courant number, defined as

$$Co = \frac{U \Delta t}{\Delta x} \tag{2.8}$$

for a one-dimensional flow, has to be below some value. The Courant number is essentially equal to the number of cells that a fluid particle passes through in a single time step. When the CFL condition is fulfilled, a suitable time step can be determined based on the ratios of local flow velocity and resolution of spatial discretization. [6]

2.5 Turbulence modelling

Turbulence is a phenomenon in fluid mechanics that translates into chaos and irregularity in fluid flows with respect to both space and time. Most fluid flows that occur in nature or industry are turbulent, which makes understanding it important when attempting to model these flows. Flows inside an engine are no exception as they can in most cases be considered very turbulent.

2.5.1 Turbulence as a phenomenon

Turbulent flow is characterized by turbulent eddies that span a large amount of sizes and magnitudes. These turbulent eddies disperse flow properties very effectively compared to laminar flow, leading to a high degree of mixing of the operating

fluid.

Existence of turbulence in each flow case can be estimated with a function of the flow case's characteristic velocity U, characteristic length scale L and the working fluid's kinematic viscosity ν. This dimensionless function is named the Reynolds number and is defined as:

$$Re = \frac{UL}{\nu}. \tag{2.9}$$

The Reynolds number can be thought of as a ratio between the inertial and viscous forces in the fluid flow. The magnitude of the Reynolds number indicates the turbulence characteristics of the flow. Higher numbers correspond to more turbulent fluctuations. Typically, a Reynolds number of a few thousands and above indicates that the flow is turbulent, but the exact point of transition is case-sensitive.

Turbulence has the property of dissipating the momentum of a flow. In a process called the energy cascade, larger turbulent eddies break into multiple smaller ones and the momentum of the original eddy is spread out across the smaller eddies. The created smaller eddies are subject to the same process, and this continues until the eddies reach a Reynolds number, where molecular viscosity dissipates the kinetic energy into heat. The rate of turbulent dissipation is denoted with ε.

The dimensions of the smallest eddies before dissipation are defined by the Kolmogorov scales for length, velocity, and time and are derived from the kinematic viscosity and turbulent dissipation rate of the fluid flow:

$$\eta \equiv \left(\nu^3/\varepsilon\right)^{1/4}, \tag{2.10}$$

$$u_\eta \equiv (\varepsilon\nu)^{1/4}, \tag{2.11}$$

$$\tau_\eta \equiv (\nu/\varepsilon)^{1/2}. \tag{2.12}$$

With high Reynolds number flows, such as those in an engine, the difference between the scales of the largest flow structures and the Kolmogorov scales are of several orders of magnitude, the latter being very small compared to the characteristic scales of the case.

Modelling all of the flow phenomena of a high Reynolds number flow case would require, that the model incorporates all of the scales of turbulent motion that are present. Capturing the scales of the smallest turbulent eddies would then require the model to be very precise, much beyond the characteristic scales of the flow case modelled.

While these types of models are sometimes deployed, like direct numerical simulations (DNS) in CFD, getting results from them can be very time consuming and resource intensive. Another way of determining the effects of turbulence on a flow case is to model them statistically. An approach to turbulence modeling is to start from a realization, that while predicting the exact development of a turbulent flow field is very difficult, its mean properties over larger length and time scales can be quite predictable.

2.5.2 Reynolds decomposition

A real flow field can be thought of as the sum of its mean flow field $\langle \boldsymbol{U} \rangle$ and a field of unpredictable turbulent fluctuations $\boldsymbol{u}$, as

$$\boldsymbol{U} = \langle \boldsymbol{U} \rangle + \boldsymbol{u}. \tag{2.13}$$

This division of the real flow field into these two different fields is referred to as the Reynolds decomposition. Take the momentum equation of Navier-Stokes equations

$$\frac{D\boldsymbol{U}}{Dt} = \nu \nabla^2 \boldsymbol{U} - \frac{1}{\rho} \nabla p. \tag{2.14}$$

The substantial derivative $\frac{D}{Dt} = \frac{\partial}{\partial t} + \boldsymbol{U} \cdot \nabla$ houses the nonlinear convective terms of the Navier-Stokes equations. In the equations, these nonlinear terms account for turbulence and solving for them is nontrivial for most general cases. Taking the mean of the substantial derivative, applying the Reynolds decomposition to it and defining a mean substantial derivative $\frac{\bar{D}}{\bar{D}t} = \frac{\partial}{\partial t} + \langle \boldsymbol{U} \rangle \cdot \nabla$ leads to the mean of the substantial derivative of the real flow field being able to be written as

$$\langle \frac{DU_j}{Dt} \rangle = \frac{\bar{D}}{\bar{D}t} \langle U_j \rangle + \frac{\partial}{\partial x_i} \langle u_i u_j \rangle. \tag{2.15}$$

Here the final term houses the velocity covariances which are called Reynolds stresses. Taking the mean of the momentum equation (2.14) and inserting the relation above gives the Reynolds equations

$$\frac{\bar{D}}{\bar{D}t} \langle U_j \rangle = \nu \nabla^2 \langle U_j \rangle - \frac{\partial}{\partial x_i} \langle u_i u_j \rangle - \frac{1}{\rho} \frac{\partial \langle p \rangle}{\partial x_i}. \tag{2.16}$$

The Reynolds stress term here differentiates the momentum equations for a real flow field and a mean flow field. While Reynolds stresses aren't literal stresses like the isotropic stresses caused by the static pressure and viscous stresses, here they have an equivalent effect on the fluid. The mean pressure field $\langle p \rangle$ satisfies a Poisson equation similarly to static pressure

$$-\frac{1}{\rho} \nabla^2 \langle p \rangle = \frac{\partial \langle U_i \rangle}{\partial x_j} \frac{\partial \langle U_j \rangle}{\partial x_i} + \frac{\partial^2 \langle u_i u_j \rangle}{\partial x_i \partial x_j}. \tag{2.17}$$

Turbulent kinetic energy is the mean kinetic energy per unit mass in the fluctuating velocity field. It is given the definition of

$$k = \frac{1}{2} \langle \boldsymbol{u} \cdot \boldsymbol{u} \rangle = \frac{1}{2} \langle u_i u_i \rangle. \tag{2.18}$$

The isotropic part of the Reynolds stress tensor is therefore $\frac{2}{3} k \delta_{ij}$ and the deviatoric anisotropic part $\langle u_i u_j \rangle - \frac{2}{3} k \delta_{ij}$. Analogously to the stress–rate-of-strain relation for a Newtonian fluid, the turbulent viscosity hypothesis states that the deviatoric Reynolds stress is proportional to the mean rate of strain caused by the turbulent fluctuations

$$-\rho \langle u_i u_j \rangle + \frac{2}{3} \rho k \delta_{ij} = \rho \nu_T \left(\frac{\partial \langle U_i \rangle}{\partial x_j} + \frac{\partial \langle U_j \rangle}{\partial x_i} \right). \tag{2.19}$$

Inserting this into Reynolds equation (2.16) with the statement that the effective viscosity is equal to the sum of kinematic viscosity and turbulent viscosity $\nu_{eff} = \nu + \nu_T$ gains the equation

$$\frac{\bar{D}}{\bar{D}t}\langle U_j\rangle = \frac{\partial}{\partial x_i}\left[\nu_{eff}\left(\frac{\partial\langle U_i\rangle}{\partial x_j} + \frac{\partial\langle U_j\rangle}{\partial x_i}\right)\right] - \frac{1}{\rho}\frac{\partial}{\partial x_j}\left(\langle p\rangle + \frac{2}{3}\rho k\right). \tag{2.20}$$

This equation doesn't have the problematic Reynolds stress term, but instead the unknown effective viscosity. The value of the effective viscosity and correspondingly the turbulent viscosity can be approximated using models.

The turbulent viscosity hypothesis has been shown to be inaccurate for many flow cases [7]. For simple shear flows however, it can produce results that have good agreement with reality.

2.5.3 Turbulent viscosity models

To solve the mean-momentum equation incorporating the turbulent viscosity hypothesis (2.20), a model has to be used in order to have a value for ν_T. The simplest turbulent viscosity models are algebraic models, such as the mixing length model. The next step in complexity would be a one-equation model where one equation, for k for example, is solved. In both cases a mixing length l_m has to be defined by the modeller. This is problematic, as the mixing length is not easily definable for most flow cases and the definition usually requires a lot of guesswork. The lack of definition for the mixing length means that the models are incomplete. [7]

Two-equation models are the simplest turbulent viscosity models that can be complete. This means that there is no need to define flow-specific parameters such as the mixing length. Two-equation turbulent viscosity models have been the industry standard for a long time and are able to produce good results and that's why they're also considered here.

The k–ε model

The k–ε model is the most widely used two-equation turbulence model. It is based on the turbulent viscosity hypothesis and in it model transport equations for both turbulent kinematic energy k and turbulent dissipation rate ε are solved. In the k–ε model turbulent viscosity is defined as

$$\nu_T = C_\mu \frac{k^2}{\varepsilon} \tag{2.21}$$

where C_μ is a model constant. The model transport equation for k is

$$\frac{\bar{D}k}{\bar{D}t} = \nabla\cdot\left(\frac{\nu_T}{\sigma_k}\nabla k\right) + \mathcal{P} - \varepsilon \tag{2.22}$$

and for ε

$$\frac{\bar{D}\varepsilon}{\bar{D}t} = \nabla\cdot\left(\frac{\nu_T}{\sigma_\varepsilon}\nabla\varepsilon\right) + C_{\varepsilon 1}\frac{\mathcal{P}\varepsilon}{k} - C_{\varepsilon 2}\frac{\varepsilon^2}{k}. \tag{2.23}$$

Here $\mathcal{P}$ denotes the production of turbulent energy which is calculated with $2\nu_T \bar{S}_{ij}\bar{S}_{ij}$, where $\bar{S}_{ij} = \frac{1}{2}\left(\frac{\partial\langle U_i\rangle}{\partial x_j} + \frac{\partial\langle U_j\rangle}{\partial x_i}\right)$ is the mean rate of strain, σ_k,σ_ε are the turbulent Prandtl numbers for kinetic energy and dissipation respectively, and $C_{\varepsilon 1}$, $C_{\varepsilon 2}$ are model constants. The standard values for all of the model constants and Prandtl numbers have been determined as

$$C_\mu = 0.09, C_{\varepsilon 1} = 1.44, C_{\varepsilon 2} = 1.92, \sigma_k = 1.0, \sigma_\varepsilon = 1.3 \tag{2.24}$$

with a numerical study [8].

The k–ω model

The k–ω model is a two-equation turbulent viscosity model that solves k with equation (2.22) similarly to the k–ε model, but instead of ε, $\omega \equiv \varepsilon/k$ is solved with the equation

$$\frac{\bar{D}\omega}{\bar{D}t} = \nabla \cdot \left(\frac{\nu_T}{\sigma_\omega}\nabla\omega\right) + C_{\omega 1}\frac{\mathcal{P}\omega}{k} - C_{\omega 2}\omega^2 + \frac{2\nu_T}{\sigma_\omega k}\nabla\omega \cdot \nabla k. \tag{2.25}$$

2.5.4 Large eddy simulation

Large eddy simulation (LES) stands as a compromise between the computational efficiency of Reynolds stress turbulence models and accuracy of DNS. In LES, the major energy-containing large turbulent fluctuations are resolved, but smaller dissipative fluctuations are modelled. The small fluctuations in fluid flow are unproportionally expensive to resolve when compared to their effect on the mean flow, as they require much smaller spatial and temporal resolutions in order to be resolved. [7]

A filtering process is used to divide the flow field into a filtered part, which is supposed to represent the large eddies, and a residual part which contains the rest. The filtered part is determined by convolution with a filter function

$$\overline{U}(x) = \int_{-\infty}^{\infty} G(r)U(x-r)dr. \tag{2.26}$$

There are many different filter functions which have their own benefits and drawbacks. The residual part is calculated simply with

$$u' = U - \overline{U}. \tag{2.27}$$

By applying the filtering to the momentum conservation equation gives

$$\frac{\partial\overline{U}_j}{\partial t} + \overline{U}_j\frac{\partial\overline{U}_j}{\partial x_i} = \nu\frac{\partial^2\overline{U}_j}{\partial x_i\partial x_i} - \frac{\partial\tau_{ij}^r}{\partial x_i} - \frac{1}{\rho}\frac{\partial\overline{p}}{\partial x_j}. \tag{2.28}$$

The equation contains the anisotropic residual stress tensor τ_{ij}^r which has to be modelled to close the equation. The Smagorinsky model is the simplest such model.

3

Literature review

3.1 Model validation in CFD

Validation is the process of assessing how well a model solution corresponds to real world phenomena. In this thesis models and parameters used in engine CFD modelling are compared to each other and validated to experimental, real world results. A problem with getting data from real world phenomena is that it always requires explicit measurements from quantities that can be measured. In CFD, there are a lot of quantities of interest that are not physically measurable, such as turbulent kinetic energy. Directly assessing the validity of such quantities is not possible, which makes the validation process more difficult. In this section previous CFD validation studies are looked into.

Validation methods in CFD were discussed extensively in [9]. A topic that was discussed and is highly relevant for this thesis is that of the validation metric. The stated features of a validation metric include having to incorporate an estimate of the numerical error, including all uncertainties caused by modelling assumptions, an estimation of random errors in experimental data, an estimation of random errors in experimental data, depending on the number of experimental replications, and incorporating random uncertainty in experimental parameters and lack of experimental results in computational quantities. In cases where experimental measurement error is zero, the experimental data and modelled results can be directly compared to create a validation metric, as long as there is a model solution at the locations of experimental measurements. The stated advantages for a validation metric are normalization in order to create a relative error norm, making sure that there are not both positive and negative errors that could offset each other, but all error would be of the same sign, and that the metric clearly indicates when model results agree with the experimental measurements and when not. It is also discussed that for engineering purposes specifying a limit for a validation metric that would divide model solutions to valid or invalid is not valuable as for engineering, validation is an estimation problem. Validation should also be separate from qualification, which discusses the ability of a model to adequately predict the phenomena it is intended for.

Numerical tests of a dual-fuel engine were performed and validated against experimental results [10]. The simulations were run using KIVA-3V code for a three dimensional engine modeled with a diesel-methane fuel mixture. An experimental

engine rig was used to obtain measurements to validate the simulation results. Two different test cases were run, the other with a premixed ratio of 22% comparing the engine running at 1500 rpm and 2000 rpm. The second case was running at 2000 rpm and compared premixed ratios of 18% and 22%. From the experimental engine rig, the in-cylinder pressure values were measured at 0.2 crank angle intervals and spectroscopic measurements of the spatial distribution of OH were taken. The curves of simulated and experimental in-cylinder pressures as functions of crank angle were visually compared with good agreement. The total fuel burning rate of the simulation and the measured OH radical formation were also compared and the starts of their activities during the cycle process lined up perfectly.

Different turbulence models were compared and validated against experimental values for several simple flow cases [11]. The two-equation model $k - \varepsilon$, $k - \omega$, and SST and the one-equation Sparalt-Allmaras model were turbulence models subject of study. The basic flow cases on which the turbulence models were tested on were a mixing layer, plane jet, round jet, plane wake, compressible mixing layer, incompressible boundary layer, axisymmetric boundary layer with adverse pressure gradient, transonic separation flow over an axisymmetric bump and transonic airfoil, all of which had experimental data available that could be used in the validation. The turbulence models' ability to predict different flow properties acted as the main tool of comparison and the properties in question depended on the case. For example, for the mixing layer case velocity profiles and spreading rates were studied. Sensitivity analyses for each turbulence model were performed by incrementing simulation parameters, such the size of the computational grid, different values of freestream eddy viscosity or using different numerical codes and the sensitivity of simulation results to these changes was documented and plotted against experimental values. For each case, an analysis was provided that discussed the modelling accuracy of each turbulence model for each flow case.

The European Research Community on Flow, Turbulence and Combustion (ERCOFTAC) provides a "Classic Collection" database which collects experimental and validated high-fidelity numerical data of different flow cases and links to the relevant research [12]. Currently the database is administered by the CFD and Turbulence Mechanics research group in the School of Engineering at The University of Manchester and the data is openly available for anyone interested. Since 1992 the database has collected entries from authors who have wanted to give results from their research to open use. Databases such as the one provided by ERCOFTAC can be used to find reliable data for validating CFD studies. There are also many other similar databases that are administrated by universities or administrations, such as [13], [14] and [15].

3.2 Imperial College case

The Imperial College case [1] refers to an experimental engine setup where the turbulent flow data inside an engine cylinder is measured using laser-Doppler anemometry. This experimental data can be used to validate numerical results.

3.2.1 Experimental setup

A plexiglass piston-cylinder is set under motored conditions while connected to an air source that has atomized silicone-oil droplets mixed in. Laser beams are shone through the engine in order to illuminate the droplets.

In laser-Doppler anemometry a laser beam is shone through an optical system that has a rotating grating diffractor component. When the beam passes the grating, the resulting interference pattern resembles a symmetric array of beams of varying angles and intensities. The grating having motion to a perpendicular direction to the original beam creates a Doppler effect to the diffracted beams. Beams that have a direction component parallel to the direction of motion of the grating have their frequencies increased and the beams with an opposite direction component to the motion of the grating have their frequencies reduced. [16]

In the case of the Imperial College case, only the first order diffracted beams are allowed to pass through a mask into a lens to be focused into the engine cylinder. The light that scatters from the silicone-oil droplets is then captured. By inspecting the change in the locations of the individual silicone-oil droplets in time, the magnitude and direction of their velocity can be approximated. Due to the small mass and size of the droplets, their velocity can be assumed to be the same as for the flow field at the same location.

There were three different engine configurations for which the experiment was done. One, shown in figure 3.1b, had air entering through a centrally located pipe with an inner diameter of 18.75 mm and a length of 1.8 m, and the two others, shown in figures 3.1a and 3.1c, had annular ports with a 30° angle of entry. The port had an outer diameter of 33.65 mm with a 4 mm uniform gap and length of 7.5 mm. The difference between the second and third arrangement was that the other had a plane piston head, whereas the other had a piston bowl.

The experiment was carried out multiple times, and the final approximations of flow axial velocity fields inside the engine cylinder were done by ensemble averaging between cycles. Also, the root mean square (rms) between differences of each cycle to the mean velocity field was taken as it can be interpreted as being analogous to turbulence levels. The data is provided for four different crank angles, 36, 90, 144 and 270 degrees and for three different engine geometries with two different air inlets and two different piston geometries for the annular air inlet.

3.2.2 Numerical studies

A direct numerical simulation (DNS) was performed based on the Imperial College case [17]. An accurate 3D geometry was created representing the engine cylinder with the annular port and flat piston head used in the Imperial College experiments. A high-order spectral element incompressible flow solver was used.

The computational grid consisted of 168 564 conforming hexahedral spectral ele-

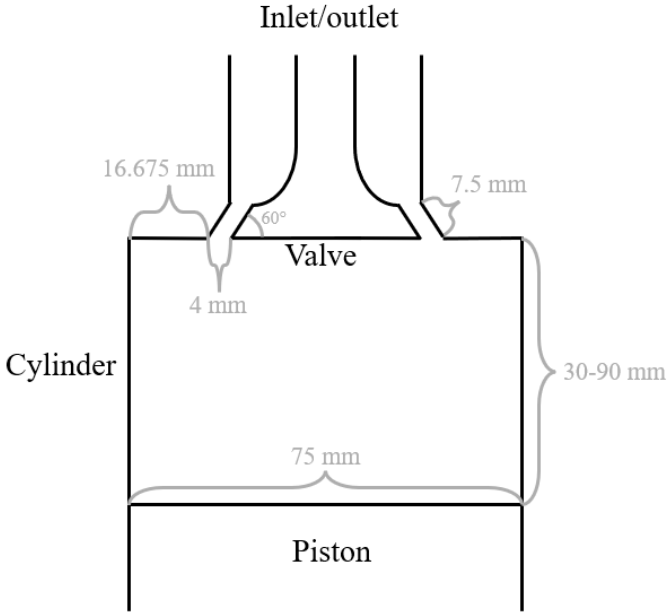

(a) Configuration with an annular port and a flat-headed piston.

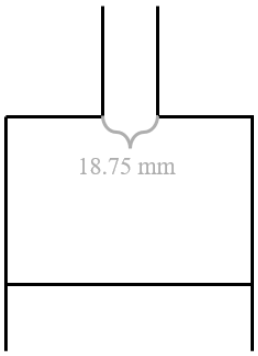

(b) Configuration with a straight pipe entry.

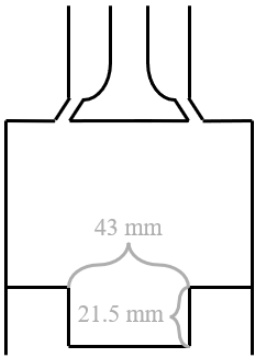

(c) Configuration with an annular port and a piston with a bowl.

Figure 3.1: The three different configurations of the Imperial college engine experiment [1].

ments with a polynomial order of $n = 7$ equating to $57.8 \cdot 10^6$ discretization points. The grid in question was chosen out of four options of different resolution with a study that compared autocorrelation of vorticity magnitude, mean and rms of axial velocity. The chosen grid was the second highest in resolution but showed great conformity to the results of the highest resolution grid, unlike the two coarser grid options.

The simulations were run for multiple cycles. There were large differences in flow fields between cycles, so different averaging methods were used to have results be more representative of the general flow characteristics. As the engine cylinder was axisymmetric, azimuthal averaging could be done to represent the instantaneous flow phenomena in a single 2D slice. Ensemble averaging was done to combine the data from different cycles.

Ensemble and azimuthally averaged axial velocity profiles and the rms of the az-

imuthally averaged axial velocities from different cycles from the simulations were compared to the experimental results of the Imperial College case. Good agreement with the experimental data was found in the later cycles of the simulation, which were less affected by the initial conditions. The ensemble averages of axial velocity were in good agreement. The rms values generally had good agreement with the experimental values.

Due to the accuracy of the results of the DNS simulation with the experimental results, the DNS simulation results can be used to represent the experiment with good confidence. While the experimental results are the most accurate representation of the physical phenomena of the case, they are quite sparse in resolution and the number of physical parameters. From the DNS results the whole flow field can be inspected in very high resolution and for multiple physical parameters.

While the DNS simulation produces very high-quality results, it's not practical to do multiple ones with different simulation parameters due to its extremely high computational cost. The results can however be used to calculate quantities that are in other cases approximated with models such as Reynolds stresses and turbulent kinetic energy. Simulations done using RANS or LES turbulence models can then be validated using the fields calculated with DNS. [3]

Similarly, a large eddy simulation (LES) study based on the Imperial College case was performed [18]. The study was done also using the engine cylinder configuration with the annular port and flat piston head. Simulations were done with OpenFOAM using finite volume method and the wall-adapting local eddy-viscosity (WALE) subgrid-scale model was included.

A mesh with approximately 4,8 million cells was used. For the inlet and outlet plenum parts and inside the cylinder near the port the mesh was static. Further down the cylinder up until the piston head the mesh was set to dynamically scale according to the movement of the piston, while cell count stayed constant.

The simulation was run for ten crank cycles. Firstly, volume averaging was done over the circumference of the engine cylinder and then ensemble averaging and root mean squares of axial velocity volume averages over the last eight cycles. After this process, the simulated data was compared to the experimental data of the Imperial College experiment.

For the crank angles 36°, 90°, 144° and 270°, for which experimental results were available, the simulated results generally showed good agreement with both the axial velocities and the root mean squares. However, an outlier was crank angle 90° which had noticeable differences in axial velocities and streamline plots between simulated and experimental results.

A completeness estimation was performed on the results using a length scale resolution (LSR) parameter. The LSR parameter is the ratio between actual resolved

turbulent kinetic energy level and the corresponding lower limit of the inertial subrange. An LSR value of around five is the upper limit for a reasonable LES resolution. The completeness estimation showed that only for some parts of crank angle 90° did the LSR reach over five, which was assumed to be the explanation for differences with axial velocities and streamlines for that instance. Even in that case, the LSR was sufficiently low that it would not cause significant problems for the overall simulation.

4
Methodology

This section looks at the different methodologies that are used for the studies conducted in this thesis. Mainly, this includes the definition of the engine model being used in the simulations, as well as the methods that are used in post-processing and analyzing the results of the study.

4.1 Engine model definition

The engine model used for the simulations is based on the Imperial college experiment [1] and more specifically the setup with an annular port and a flat piston head. The basic model used in this thesis is created by Wärtsilä and uses in-house meshing utilities that have been automated and parallelized. The geometry of the engine model is presented in figure 4.1. The model is axisymmetric and mostly follows the dimensions of the experimental engine except for the port between the inlet and the valve which has been elongated for modelling purposes. There is one patch at the top of the model that acts as an inlet and an outlet. Other patches are either moving or stationary walls.

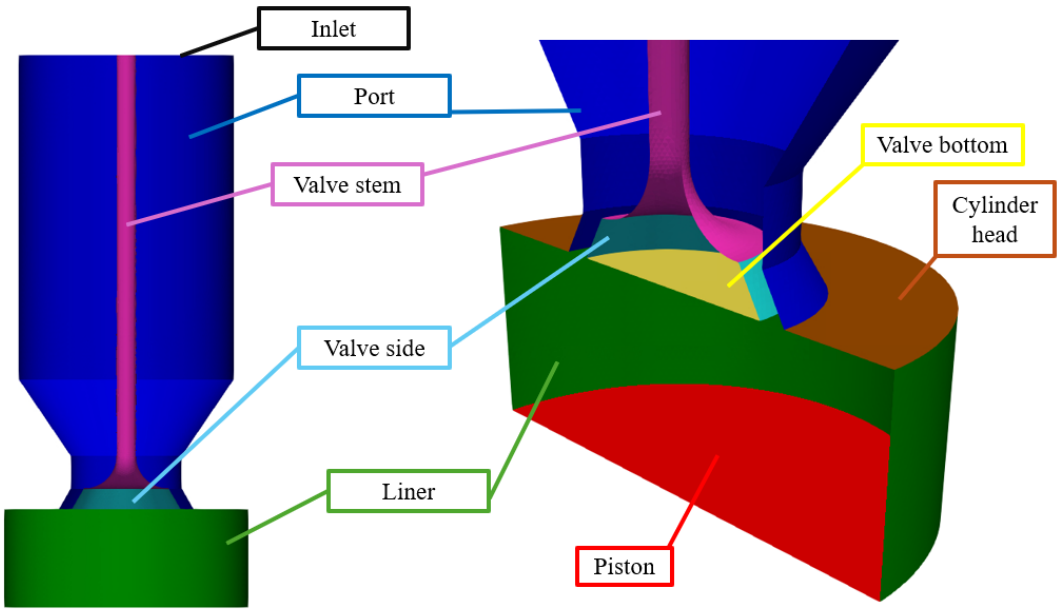

Figure 4.1: Cross-section of the engine model and its patch definitions.

An essential part of the engine operation is the cyclical movement of the piston.

This is taken into account in the model by the piston patch moving up or down in the same way as in the experiments. The motion of the piston is calculated for each time instance based on the rpm of the engine, which is 200, and the stroke which is 6 cm with

$$U_{piston}(t) = \frac{dz_{piston}}{dt} = \frac{d}{dt}\left(\frac{1}{2}s_e \cdot sin(\omega_e t)\right) = \frac{1}{2}s_e\omega_e \cdot cos(\omega_e t)$$

$$\approx 0.628\frac{m}{s} \cdot cos(20.9\frac{1}{s} \cdot t). \tag{4.1}$$

In addition to the piston patch having translational movement, the liner patch is continuously scaled so that it is connected to both the cylinder head and piston patches.

4.1.1 Meshing

A structured hexahedral mesh is created for the engine model with a base mesh size of 4 mm. Volumetric refinement of multiple levels is applied to the mesh. In this case, a level of refinement translates to hexahedral cells being divided into eight smaller cells of equal size and with further levels this procedure is subsequently done to smaller cells. A transition between refinement levels in the mesh is always gradual, so adjacent cells have a maximum of one level of difference between their refinement levels. The mesh near all surfaces is refined to level 2, so twice. Additionally, the mesh near the valve object surface is refined to level 4, the whole of the cylinder volume is refined to level 2 and there is a conical refinement region that goes over the valve port and 10.4 mm down the cylinder volume starting from the valve port opening of level 3. Finally, near the piston surface the refinement level is 3. Inflation layers are also used in the mesh. All surfaces have at least one inflation layer. On the valve object and piston surfaces, there are two inflation layers. The mesh is presented in figure 4.2 with the refinement levels and inflation layers visible.

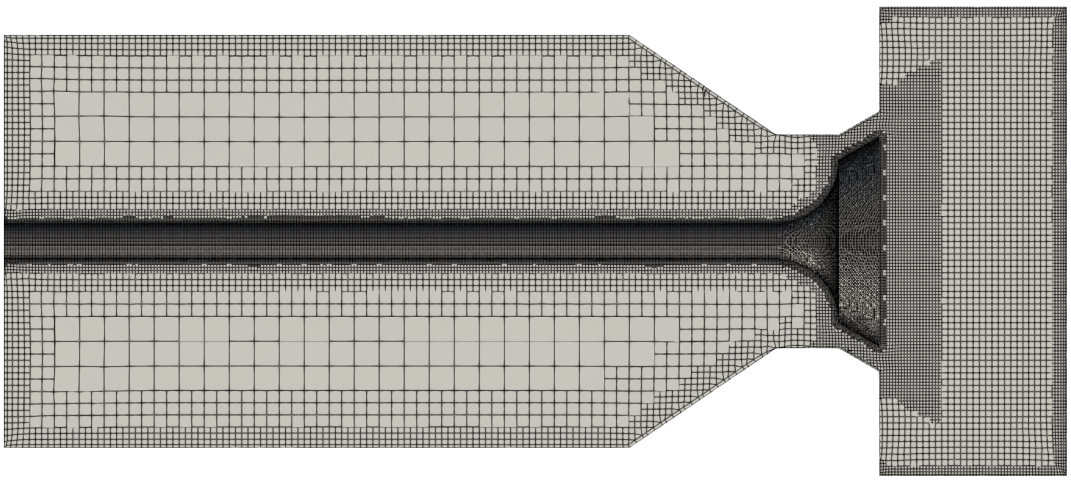

Figure 4.2: Cross-section of the computational mesh for the engine model.

Since the piston patch moves during the simulation and the cylinder expands and contracts, the mesh has to also conform to these changes. This is done in two different procedures. Firstly, 13 different meshes are created based on the aforementioned meshing options for different crank angle instances ranging from 0° to 720°. These different meshes have different amounts of cells. Secondly, between the crank angle instances, the cells inside the cylinder are scaled corresponding to the transformation of the cylinder volume using a mesh mover.

When the mesh is changed to a new one, the values for the new cells are calculated based on the previous ones. If only the second procedure was used, cells would become very elongated or flattened during the cycle process, which isn't desirable. For this reason, the mesh-to-mesh mapping is carried out at specified times. On the other hand, doing a separate mesh for each time step would require an excessive amount of meshes. Also, as calculating the field values from the previous mesh to a new one always produces some error, doing it for every time step wouldn't be a good idea.

4.1.2 Choices for models and parameters of interest

The Imperial college case engine model has some initial choices for models and parameters that were made by the authors of the base model. These choices act as the defaults for the simulations in this thesis, unless specified otherwise.

Boundary and initial conditions

The choices for boundary conditions (BC) and initial conditions (IC) are presented in table 4.1.

Field	Wall BC	Outlet BC	IC
U	`noSlip`	`pressureInletOutletVelocity`	0
p	`zeroGradient`	`totalPressure`	101 325 Pa
T	`zeroGradient`	`inletOutlet`	293 K
ε	`epsilonWallFunction`	`inletOutlet`	277.4 m^2/s^3
k	`kLowReWallFunction`	`inletOutlet`	0.3875 m^2/s^2
ν_T	`nutkWallFunction`	`calculated`	0.0003896 m^2/s
ω	`omegaWallFunction`	`inletOutlet`	715.7 1/s

Table 4.1: Engine model boundary and initial conditions.

Solver options and numerical schemes

The algorithm used in the simulations is the PIMPLE algorithm, that combines controls from the PISO (Pressure-Implicit with Splitting of Operators) and SIMPLE (Semi-Implicit Method for Pressure-Linked Equations) algorithms [6]. Matrix equations for different fields are solved with either PBiCGStab (Preconditioned Bi-Conjugate Gradient Stabilized) or PCG (Preconditioned Conjugate Gradient).

The numerical schemes used in the simulation for time differential (d/dt), gradient ($\Delta\Psi$), advection ($\nabla\cdot(U\Psi)$), Laplacian ($\Gamma\nabla_n\Psi$) and interpolation operations are listed in table 4.2. A noticeably intricate scheme is the one for velocity advection, which has been deemed effective in the in-house simulations at Wärtsilä. It is a blended scheme of which behavior is based on the local Courant number.

Operator	Field	Scheme
d/dt	default	`Euler`
$\Delta\Psi$	default	`Gauss linear`
	U	`cellLimited Gauss linear 1`
$\nabla\cdot(U\Psi)$	default	`Gauss limitedLinear 1`
	U	`Gauss cellCoBlended 2 limitedLinearV 1 4 upwind`
	k, ε, ω	`Gauss upwind`
$\Gamma\nabla_n\Psi$	default	`Gauss linear limited corrected 0.333`
Interpolation	default	`linear`
	Co	`localMax`

Table 4.2: Numerical schemes used for different operators.

Turbulence model

The engine model uses the Re-normalization group (RNG) $k-\varepsilon$ turbulence model, which tries to better account for the effects of the smaller scales of turbulence compared to the standard $k-\varepsilon$ model [19].

Time step and maximum Courant number

The time step length in the simulations is not constant and is instead calculated based on a set maximum for the Courant number. After each time step, based on the previously solved velocity field, and the current mesh dimensions, a time step length is chosen so that the calculated Courant number for each point in the simulated volume is at most the given maximum Courant number. The default value for the maximum Courant number used in the simulations is 4.

4.2 Benchmarking

The results from the Imperial college case simulations needed to be post-processed in order to effectively validate them against reference data. The experimental results [1] were given as two-dimensional profile data that was ensemble averaged between cycles. Profiles of axial velocity, rms of velocity fluctuations and streamline patterns were given.

A validation study of DNS with the Imperial college case [17] was performed and similarly to the simulations performed for this thesis, they produced three-dimensional data that needed to be post-processed into two-dimensional data in order to validate towards the experiments. This was done through two distinct averaging procedures,

azimuthal averaging which turns the three-dimensional flow field into an averaged slice of the engine cylinder and ensemble averaging, which acts to create mean fields less effected by cycle-to-cycle variance. The latter was also done in the original experiments.

As the DNS results had very good agreement to the experimental results, they are also used in the validation process. Due to the much higher resolution and scope of the DNS data compared to the experiment data, it allows for a much more detailed inspection of the differences between the solutions. It is also not reasonable to expect that lower fidelity methods, such as the ones used in this thesis, would be able to outperform DNS results, but rather that the DNS results should be the absolute benchmark for what could be achieved with lower fidelity numerical methods.

4.2.1 Averaging

Similar methods of averaging to [17] are used in this thesis to post-process the data produced by the simulations. Horizontal cut planes of the computational grid inside the engine cylinder model are taken using OpenFOAM's `surfaces` function. Values from the cells within the planes are recorded at crank angles 36°, 90°, 144° and 270° for each cycle, corresponding to the experiments. The locations of the planes for each crank angle are measured as the distance below the engine port and are presented in table 4.3. There is no data for 270° in the DNS results, so it will not be considered in the averaging procedures. 270° is the only one of the crank angles that is at the suction part of the cycle and the flow structures at that part are very simple.

Crank angle	Plane distances from engine port (mm)
36°	10, 20, 30
90°	10, 20, 30, 40, 50, 55
144°	10, 20, 30, 40, 50, 60, 70, 77.5
270°	10, 20, 30, 40, 50, 55

Table 4.3: Vertical locations for sampling planes for a set of crank angles.

The data collected from the cut planes is further post-processed using a python script. One of the two main averaging procedures is azimuthal averaging. For a circular set of data, like the discs that are formed as the engine cylinder is cut using the cut planes, azimuthal averaging is performed by going around the disc in the azimuthal direction, calculating the average for each isoradius of the disc. This forms a one-dimensional set of averaged values from the center to the edge of the disc.

The computational grid used for the simulations is a structured cartesian mesh, which makes it nontrivial to perform the azimuthal averaging procedure. There are multiple ways of approaching this problem. One way would be to place isoradius circles on top of the cartesian data and calculate the average between the cells that

the isoradius circle intersects. This would be sensitive to the differences of the number of cells in the different parts of the disc, as for the parts of the disc that have a higher cell density would result being weighed higher in the average, which isn't desirable.

Another approach would be to create a regular polar coordinate system matching the dimensions of the disc and interpolate the values of the cartesian grid onto the polar grid. Azimuthal averaging for a polar grid is trivial as the number of cells under each isoradius is constant. The average is calculated with

$$\langle \Psi_i^c \rangle_\varphi = \frac{1}{n} \sum_{j=1}^{n} \Psi_{ij}^c, \tag{4.2}$$

where i is the radial index and j the azimuthal index in the polar coordinate system, c is the cycle number and n is the number grid points in the azimuthal direction. Although this method does introduce interpolation error, the amount of error can be reduced by refining the polar grid. This method is chosen to be used for azimuthal averaging in this thesis and linear interpolation is the method of choice for interpolating the data from cartesian to polar coordinates. The interpolation is performed using SciPy's `griddata` function. The same polar grid is used for all azimuthal averaging, regardless of the position or crank angle of the sample disc.

The second main averaging procedure is ensemble averaging. As in this case the all of the sample data is interpolated onto the same polar grid, the resulting dataset is also similarly spaced between different cycles. This means that the ensemble averaging is no more complicated than creating a single dataset from all the cycles by

$$\langle \Psi_{ij} \rangle_E = \frac{1}{N} \sum_{c=1}^{N} \Psi_{ij}^c, \tag{4.3}$$

where N is the number of cycles. Data that has been both azimuthal and ensemble averaged is denoted by $\langle \langle \Psi_i \rangle_\varphi \rangle_E = \langle \langle \Psi_i \rangle_E \rangle_\varphi = \overline{\Psi}_i$. This results in sets of one-dimensional azimuthal and ensemble averaged data that can be directly compared with the experimental results [1] or the DNS results [17].

4.2.2 Flow properties of interest

The flow properties that are available in the experimental measurements by [1] are the ensemble averaged vertical velocity and the rms of vertical velocity. In [17] the DNS results are also validated against the previously mentioned flow properties from the experiments and the data for these properties is available from the DNS. In addition, azimuthal and ensemble averaged TKE profiles are available from the DNS at the same crank angles and locations. These are the flow properties that the simulations done in this thesis are validated against.

Creating the azimuthal and ensemble averaged vertical velocity field $\overline{U}_z$ is very simple. The averaging procedures from section 4.2.1 are applied directly to the vertical

velocity fields that are sampled with the cut planes. Likewise to the experiments and DNS, the resulting profile is normalized with the mean piston speed from the experiments, which is $U_{p,mean} = 0.4$ m/s.

Calculating the rms of vertical velocity and TKE is a bit different, and they are strongly linked together. Firstly, a division of a property into modelled and resolved parts is introduced. The modelled part of a property is calculated by a model and a good example would be the magnitude of turbulent kinetic energy approximated by a RANS turbulence model. The resolved part is calculated as the differences to the mean flow e.g. as in fluctuations. This is done regardless of whether the models used in the simulations are set to solve only a mean flow field without fluctuations. The fluctuations in this case refer to cycle-to-cycle variations if they exist and the mean flow to the ensemble averaged flow. Analogously to the Reynolds decomposition (2.13) the velocity fluctuations can be presented as

$$\boldsymbol{u}^c = \boldsymbol{U}^c - \langle \boldsymbol{U} \rangle_E. \tag{4.4}$$

The fluctuations here are assumed different for each cycle. Taking the ensemble average of equation (4.4) confirms that the ensemble average of the fluctuations is zero, which should of course be true by definition. A meaningful way to quantify the average magnitude of fluctuations between cycles would be to take a mean square of velocity

$$\boldsymbol{U}_{ms} = \frac{1}{N}\sum_{c=1}^{N} \left(\boldsymbol{U}^c - \langle \boldsymbol{U} \rangle_E\right)^2 = \left\langle \left(\boldsymbol{U}^c - \langle \boldsymbol{U} \rangle_E\right)^2 \right\rangle_E = \left\langle \left(\boldsymbol{u}^c\right)^2 \right\rangle_E . \tag{4.5}$$

Taking the square root of (4.5) gives the rms and more specifically the resolved rms $\boldsymbol{U}_{rms,res} = \sqrt{\boldsymbol{U}_{ms}}$. The resolved TKE can be calculated according to equation (2.18)

$$k_{res} = \langle k^c \rangle_E = \left\langle \frac{1}{2}\left((u_x^c)^2 + (u_y^c)^2 + (u_z^c)^2\right) \right\rangle_E$$

$$= \frac{1}{2}\left(\left\langle (u_x^c)^2 \right\rangle_E + \left\langle (u_y^c)^2 \right\rangle_E + \left\langle (u_z^c)^2 \right\rangle_E\right) = \frac{1}{2}\left(U_{x,ms} + U_{y,ms} + U_{z,ms}\right). \tag{4.6}$$

Modelled TKE is acquired as an output from the simulation software. The directional fluctuations are not modelled and thus the modelled rms is calculated with the modelled TKE instead. The following relation can be shown if the hypothetical modelled fluctuations are assumed to be equal in every direction, based on equation (2.18)

$$k_{mod} = \frac{3}{2}\left\langle (u_{mod}^c)^2 \right\rangle_E = \frac{3}{2} U_{rms,mod}^2$$

$$\Rightarrow U_{rms,mod} = \sqrt{\frac{2}{3} k_{mod}}. \tag{4.7}$$

The total values of these properties that are simulated are combinations of the resolved and modelled parts. For TKE the combination is simply

$$k_{tot} = k_{res} + k_{mod}. \tag{4.8}$$

For rms the total is calculated with

$$U_{z,rms,tot} = \sqrt{U^2_{z,rms,res} + U^2_{rms,mod}}. \tag{4.9}$$

These resolved, modelled and total properties can then be further azimuthal averaged, and in that case no special treatment is required. In the reference data, the rms values are normalized with $U_{p,mean}$ and the same is done for the simulated values. In [17] the TKE values are not normalized, but in this thesis when the TKE values are visually displayed, both reference and the simulated values are normalized with $U^2_{p,mean}$ for presentation uniformity with the other properties.

4.2.3 Validation metric

In order to validate a numerical model solution, a visual inspection of the solution against experimental results can often be deemed sufficient. The averaged profiles produced with the methods from section 4.2.1 could be used for such an inspection and that could be sufficient for a more concise study. However, in a situation where a large number of cases need to be validated and compared with each other, such as in this thesis, mere visual inspection is very impractical. Defining a validation metric allows for a much clearer quantification of the differences between cases.

As discussed in section 4.2, the DNS results by [17] are also used for validation. Although both the experimental results and the DNS results are very usable for validation by visual inspection, the DNS results are much more practical for calculating a validation metric, thanks to their much higher resolution and the inclusion of data of additional useful flow properties that were not present in the experimental results. That is also why the DNS results are used to determine the validation metric in this thesis.

The principles presented by [9] can be referred to when defining a validation metric. For the purposes of this thesis, it is assumed that the experimental measurement error is zero. That is because considering the accuracy of the experimental measurements by [1] or the validity of the DNS results by [17] is outside the scope of this thesis and because the main focus is on the mutual comparison of the simulations performed for this thesis. This means that the validation metric can be created to directly compare the DNS results, which are considered to sufficiently well represent the experimental measurements, and the results from the simulations done for this thesis.

Mean square error

Mean square error (MSE) is a loss function that can be used as a validation metric. For a property Ψ with available experimental measurements Ψ_{exp}, it is defined as

$$\langle \Psi \rangle_{MSE} = \frac{1}{N} \sum_{i=0}^{N} (\Psi - \Psi_{exp})^2. \tag{4.10}$$

The magnitude of the MSE is proportional to the amount of error between the modelled and reference datasets. The square operator in the definition of the MSE

ensures that all errors between the model and reference data are positive and that there is no offsetting of errors due to different signs. The square operator in the MSE also causes sensitivity to large variances in error. A smaller value for $\langle\Psi\rangle_{MSE}$ corresponds to a smaller error, or a better agreement.

Mean absolute error

Mean absolute error (MAE) acts also as a loss function similarly to MSE. For a property Ψ with available experimental measurements Ψ_{exp}, it is defined as

$$\langle\Psi\rangle_{MAE} = \frac{1}{N}\sum_{i=0}^{N}|\Psi - \Psi_{exp}|. \tag{4.11}$$

The MAE has many similar benefits to MSE. The absolute operator ensures that all error is positive. On the contrary, it is not sensitive to large variances in error, as the magnitude of the error doesn't change after taking the absolute. Also similarly to the MSE, a smaller value for $\langle\Psi\rangle_{MAE}$ corresponds to a smaller degree of error and better agreement.

4.2.4 Comparison studies

In this thesis simulation models and parameters for engine related flow cases are compared. The main method of comparison is a validation metric that was discussed in section 4.2.3. For the Imperial college case, multiple comparison studies are run, each of which comprises a set of comparison cases. Comparison cases are created based on combinations of simulation models or parameters. For each study, one or more simulation models and parameters are chosen to be the variables of the study, and for each model and parameter, a few different options are chosen. These options form a matrix of cases, each with a different combination of models and parameters. After running the cases, post-processing the results and calculating the validation numeric for each case, the effectiveness of each model and parameter combination can be assessed.

Creating all the cases with different model and parameter options in OpenFOAM can be done completely manually, but it can be very laborious and prone to errors. A bash script was created in order to efficiently and reliably create all the combinations. It takes as an input all the models and parameters that are to be varied, all the different options that are given for the models and parameters, and the base case. It then copies the base case as many times that there are combinations and systematically modifies each case to include the correct model and parameter options.

Number of cycles

The suitable number of cycles for the Imperial college comparison studies was determined with a study. In order to minimize computational cost, as little number of cycles as possible should be run. However, in order to reduce the impact of statistical inaccuracy and have the simulation results agree better with reference data,

more cycles should be included in the averaging process. For engine modelling cases where the initial conditions don't resemble the operating conditions of the engine, the first couple of cycles will likely also be inaccurate due to the lingering effect of the initial conditions. To find a suitable number of cycles that are modelled, the number of first cycles that have clear influence of initial conditions should be determined added to a number of cycles that are required to reduce the amount of statistical inaccuracy significantly.

A 20 cycle run with a 4 mm base mesh size was run. The MSE between the simulated and DNS results was then calculated for each possible combination of starting cycle and final cycle. The combinations that only included one cycle showed that the first cycle was a lot more inaccurate than the other cycles and that the second cycle more inaccurate than the average cycle. For combinations where the first two cycles were omitted, less than 10 total cycles clearly showed decreasing accuracy. It was then determined that 10 cycles should be run and the first two cycles omitted from the post-processing.

4.3 Case setups for the comparison studies

4.3.1 First study

The comparison study for the Imperial college case was started with a larger parameter sweep to gain a lot of information to go forward with. In the first study, models and parameters that were initially deemed interesting were focused on. The models and parameters in question were the turbulence model, base mesh size, the numerical scheme for velocity advection and the maximum Courant number. The options that were used for these models and parameters are presented in table 4.4. The different combinations add up to $3^4 = 81$ separate cases.

Parameter	**Input**
Turbulence model	RNG $k - \varepsilon$
	$k - \omega$ SST SAS
	Standard $k - \varepsilon$
In-cylinder base cell size (mm)	1.0
	1.5
	2.0
Velocity advection scheme	`cellCoBlended 2 limitedLinearV 1 4 upwind`
	`limitedLinearV 1`
	`linearUpwind grad(U)`
Maximum Courant number	1
	4
	10

Table 4.4: Parameters for the first comparison study.

4.3.2 Second study

The second study aimed to more closely inspect the effect of the mesh resolution, with the added dimensions of the number and thickness of the surface inflation layers. The number of inflation layer has three values for each input, each for different surfaces, and this is due to there being a different number of layers on these surfaces initially, as specified in section 4.1.1. The number of layers at the valve surface is varied so that the total thickness of the layers is as close to the total thickness of the layers at the outside surface of the valve port as possible, while the expansion ratio is kept at a constant 1.2. The piston surface layers are varied so that the number of layers is one more than the global number. The thickness of the surface inflation layers is controlled by changing the relative thickness of the first layer, and the thickness of further layers is directly scaled from the first one.

The options that were used for models and parameters are presented in table 4.5. Additionally, the combination with the largest number of inflation layers and relative first layer thickness 0.50 were not considered. A visual inspection of meshes for such cases was performed and the mesh quality was very poor in all of them. The `linearUpwind grad(U)` advection scheme was used in all of the cases and maximum Courant number of 4. The different options add up to $3 \cdot 3 \cdot 2 = 15$ cases.

Parameter	Input
In-cylinder base cell size (mm)	1.0
	1.5
	2.0
Number of surface layers globally, at the valve surface and at the piston surface	1, 2, 2
	2, 3, 3
	4, 5, 6
Relative first layer thickness	0.25
	0.50

Table 4.5: Parameters for the second comparison study.

4.3.3 Third study

The third comparison study aimed to look into more turbulence models that are available in OpenFOAM, with the inclusion of inflation layer options that showed good performance in the second study. A 1.0 mm in-cylinder base cell size mesh was used with 2 global inflation layers and first layer thickness of 0.5. The same velocity advection schemes from the first study were part of the study this time as well. The maximum Courant number was 4.

Parameter	Input
Turbulence model	RNG $k-\varepsilon$
	$k-\omega$ SST SAS
	Standard $k-\varepsilon$
	Standard $k-\omega$
	$k-\omega$ 2006
	$k-\omega$ SST
	realizable $k-\varepsilon$
Velocity advection scheme	`cellCoBlended 2 limitedLinearV 1 4 upwind`
	`limitedLinearV 1`
	`linearUpwind grad(U)`

Table 4.6: Parameters for the third comparison study.

5
Results

5.1 First study

After running the simulations, and post-processing the results according to the methodology in section 4.2.1, MAEs are calculated between the results and the DNS data, for both the vertical velocity and TKE profiles. The MAE values for vertical velocity are presented in figure 5.1a and for TKE in figure 5.1b and each cell in the figures represents a case. A lower value and lighter color correspond to better agreement and vice versa. Some of the cases crashed due to numerical instability and these are blacked out in the figures. The three different meshes are presented in 5.4.

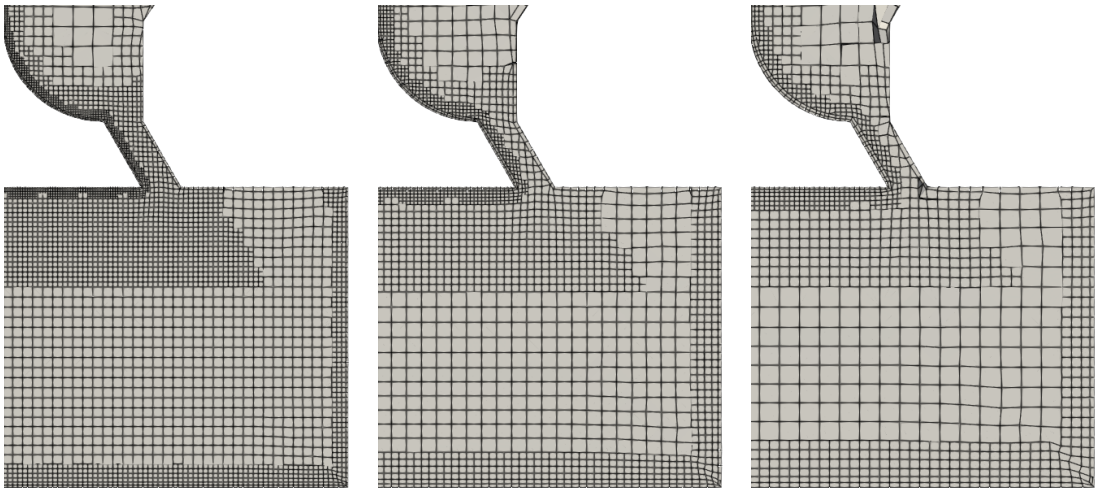

(a) 1.0 mm in-cylinder base cell size mesh

(b) 1.5 mm in-cylinder base cell size mesh

(c) 2.0 mm in-cylinder base cell size mesh

Figure 5.4: Cross sections of the meshes of the first study.

From figure 5.1a it is apparent that the vertical velocity prediction of the 1.5 mm in-cylinder base cell size cases has some noticeably poor results; either the prediction is poor or the runs have crashed altogether. The expectation would be that the results would get uniformly worse as the mesh resolution gets coarser. If the clearly unreliable results of the 1.5 mm in-cylinder base cell size are ignored, this expectation seems true for the RNG $k-\varepsilon$ and $k-\omega$ SST SAS turbulence models, but the adverse of the expectation is true for the standard $k-\varepsilon$ model, when inspecting the results for the averaged axial velocities. For averaged TKE, the expectation appears

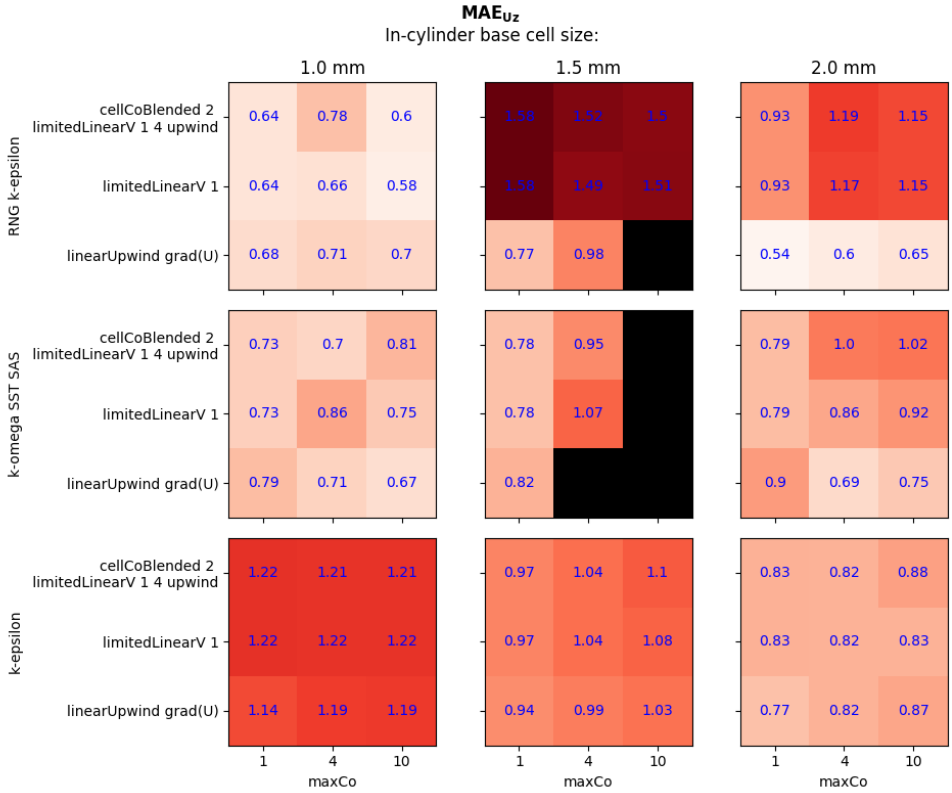

(a) Averaged axial velocity

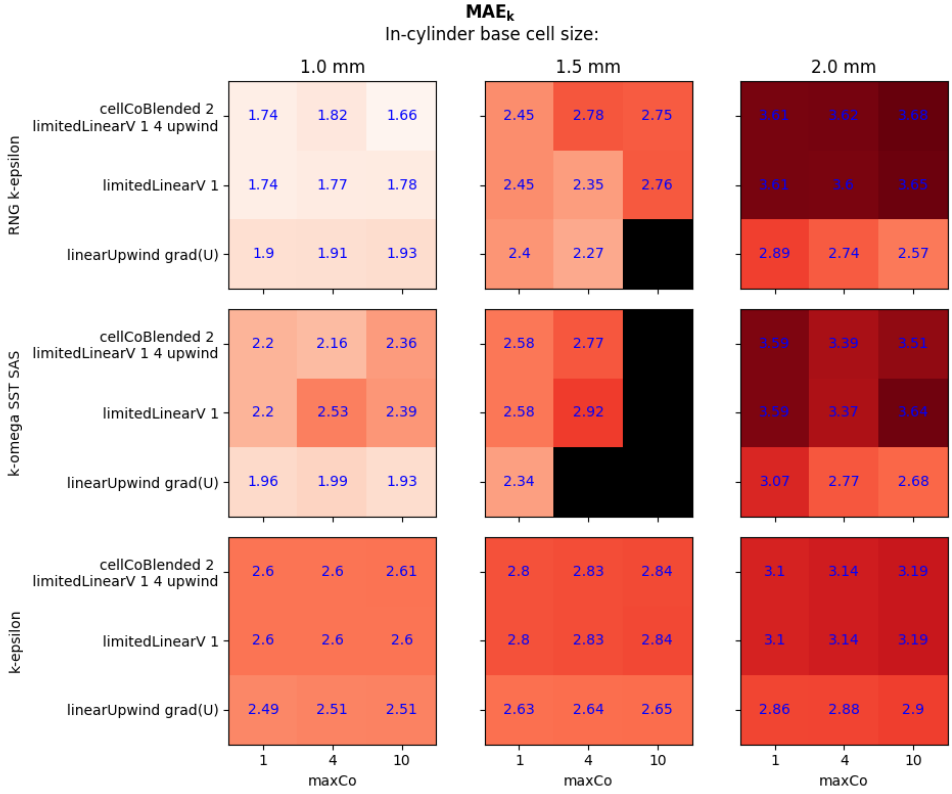

(b) Averaged turbulent kinetic energy

Figure 5.1: MAE values for the first study

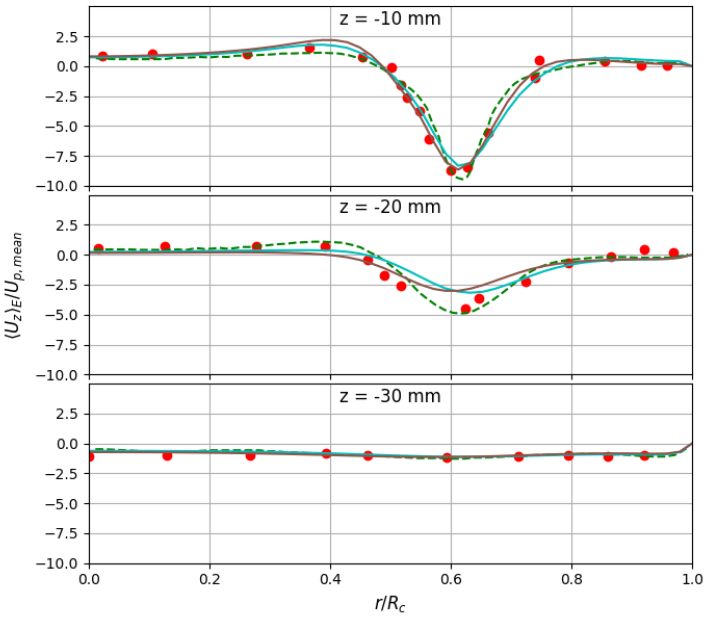

(a) 36°

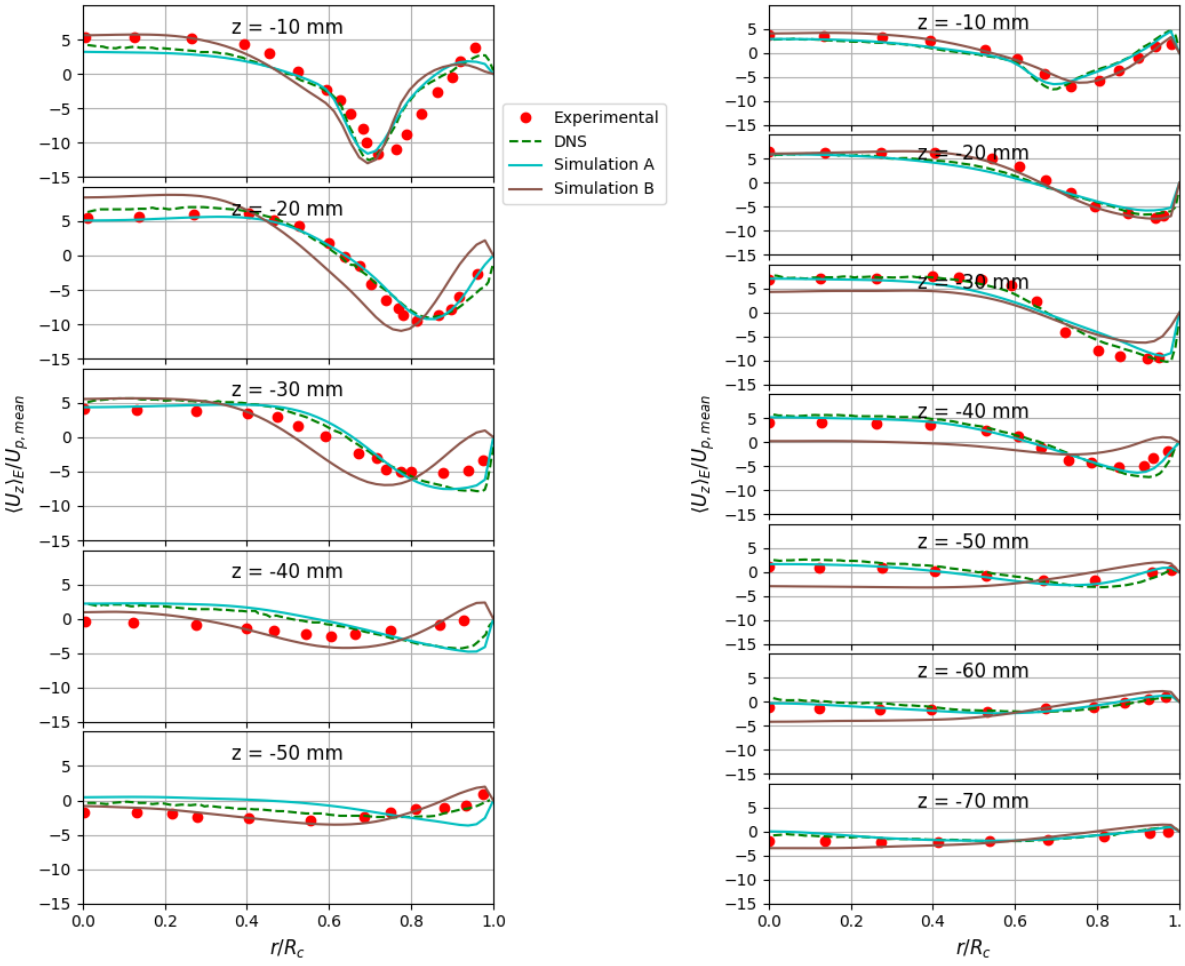

(b) 90°

(c) 144°

Figure 5.2: Averaged axial velocity profiles from the first study at specified crank angles for good case A and poor case B, compared against experimental [1] and DNS [17] values.

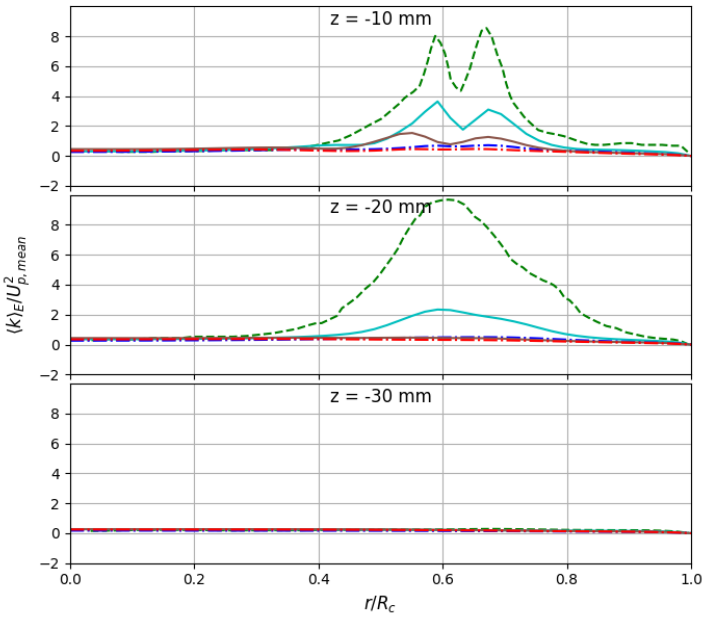

(a) 36°

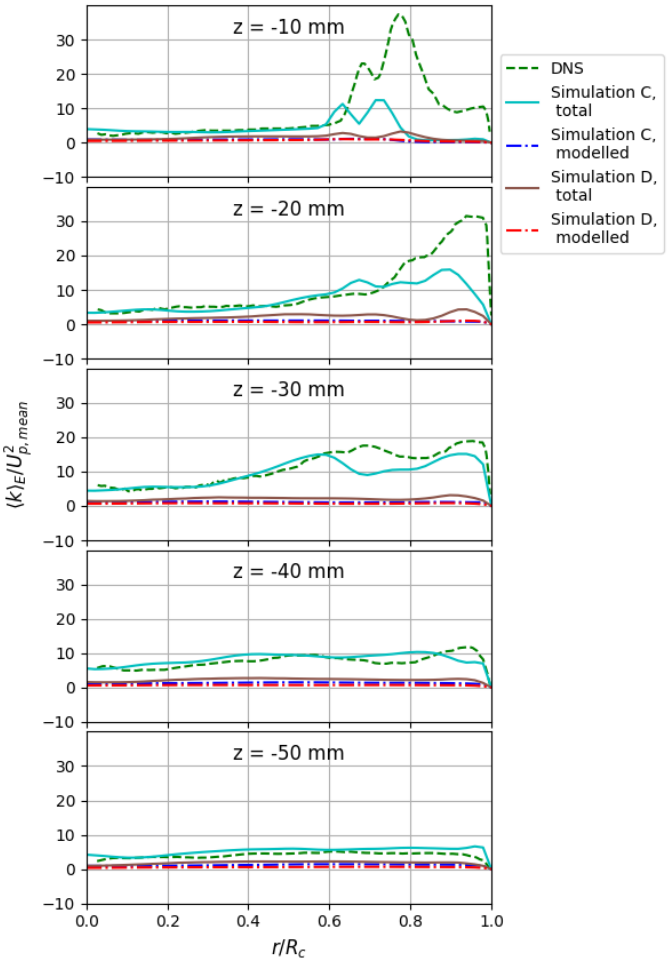

(b) 90°

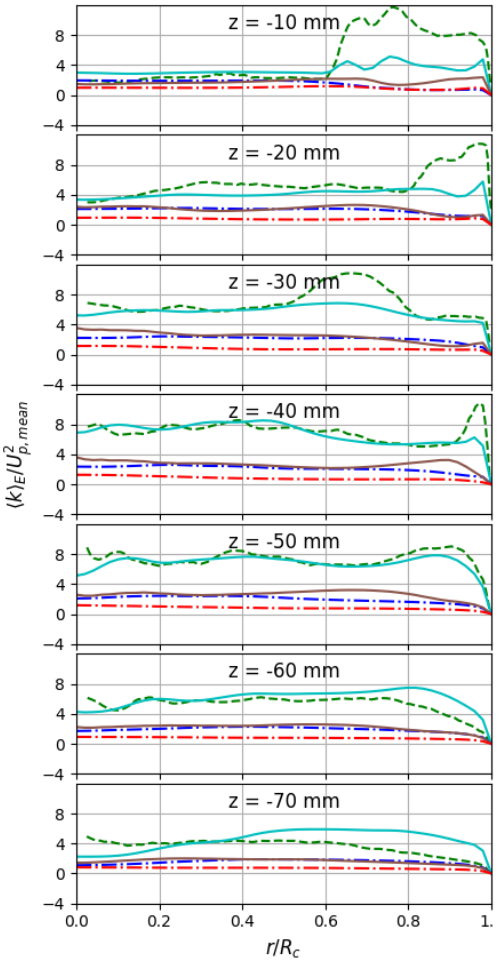

(c) 144°

Figure 5.3: Averaged total and modelled TKE profiles from the first study at specified crank angles for good case C and poor case D, compared against DNS [17] values.

to be true as can be seen in figure 5.1b. The best combination for the turbulence model and mesh resolution would be the RNG $k-\varepsilon$ with 1.0 mm in-cylinder base cell size, judging from both U_z and k results. From the turbulence models, the standard $k-\varepsilon$ gives noticeably worse results for k at the finest mesh resolution. Furthermore, in all cases its results for k seem to be the least impacted by the change in mesh resolution. The RNG $k-\varepsilon$ appears to be the most affected by changes in mesh resolution, more visibly for the U_z results than k, with $k-\omega$ SST SAS coming in second.

From the velocity advection schemes, `linearUpwind grad(U)` is performing well in all other cases, except with the combination of the RNG $k-\varepsilon$ turbulence model and the finest mesh resolution, where it is slightly worse that the other schemes. For that combination the `limitedLinearV 1` is slightly better of the two other schemes.

Overall the effect from the change in maximum Courant number is quite small, especially between values 1 and 4. However, with maximum Courant number 1, the simulation time was significantly longer. Maximum Courant number of 10 was also clearly faster than 4, but has noticeable instability with 1.5 mm in-cylinder base cell size.

Since the calculated error metrics are based on the averaged axial velocity and TKE profiles at different crank angles and distances from the valve, it would be reasonable to inspect the profiles. One good and one poor case are chosen for both averaged axial velocity and TKE based on the MAE matrices to represent the variety that can be found within the results, and their average axial velocity and TKE profiles are inspected respectively.

- For the good case with respect to averaged axial velocity, the case with RNG $k-\varepsilon$ turbulence model, 2.0 mm in-cylinder base cell size, `linearUpwind grad(U)` advection scheme and max Courant number 1 is chosen, and called case A.
- For the poor case with respect to averaged axial velocity, the case with RNG $k-\varepsilon$ turbulence model, 1.5 mm in-cylinder base cell size, `cellCoBlended 2 limitedLinearV 1 4 upwind` advection scheme and max Courant number 1 is chosen, and called case B.
- For the good case with respect to averaged TKE, the case with RNG $k-\varepsilon$ turbulence model, 1.0 mm in-cylinder base cell size, `cellCoBlended 2 limitedLinearV 1 4 upwind` advection scheme and max Courant number 10 is chosen, and called case C.
- For the poor case with respect to averaged TKE, the case with RNG $k-\varepsilon$ turbulence model, 2.0 mm in-cylinder base cell size, `cellCoBlended 2 limitedLinearV 1 4 upwind` advection and max Courant number 10 is chosen, and called case D.

The average axial velocity of cases A and B, and the TKE profiles of cases C and D, as well as the respective DNS and experimental results are presented for 36° in figures 5.2a and 5.3a, for 90° in figures 5.2b and 5.3b, and for 144° in figures 5.2c and 5.3c. Overall, the averaged axial velocity profiles for B deviate much more from the DNS results than A, but this should be obvious, as the MAE is a direct

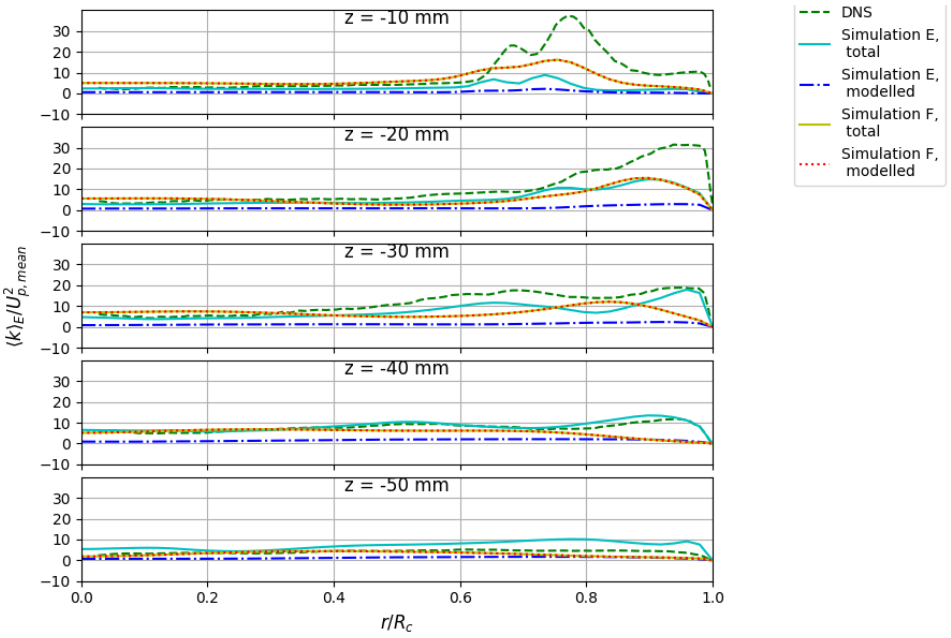

Figure 5.5: Averaged total and modelled TKE profiles from the first study at 90° for cases E and F, compared against DNS [17] values.

measure of that. Especially at 90° in figure 5.2b it is visible that the velocity profile for B has its minimum more left from that of the DNS, or closer to the center of the cylinder. The magnitude of the minimum is around the same to the DNS, so a lot of the error comes from the deviation towards the middle.

Both cases C and D predict TKE quite poorly, especially in places where the DNS TKE values are large, as can be seen in figure 5.3b, for example. In the lower parts of the cylinder at the crank angles 90° and 144°, where the DNS TKE profile is more uniform, case C is able to match it quite well, as seen in figures 5.3b and 5.3c.

Notable is that in these cases the total TKE, which consists of both the modelled and resolved TKE, is significantly larger than the modelled TKE. This means that a large portion of the TKE is resolved which in turn means that the contribution of resolved turbulent fluctuations and cycle-to-cycle variance is quite high. Cases E and F have 1.0 mm in-cylinder base cell size, `linearUpwind grad(U)` scheme and max Courant number 1, and use the $k-\omega$ SST SAS and standard $k-\varepsilon$ turbulence models respectively. Their averaged TKE profiles at 90° are presented in figure 5.5. From there it's visible that the $k-\omega$ SST SAS model acts similarly to RNG $k-\varepsilon$ with respect to the ratio of modelled and resolved TKE, whereas the standard $k-\varepsilon$ has no resolved TKE, and therefore no cycle-to-cycle variance.

Cross-sections of the instantaneous velocity magnitude fields for cases A, E and F, each representing a different turbulence model in the same mesh resolution of 1.0 mm in-cylinder base cell size at crank angles 35°, 90° and 145° of the third cycle, are presented in figure 5.6. From the fields it is very visible how much more fluctuations

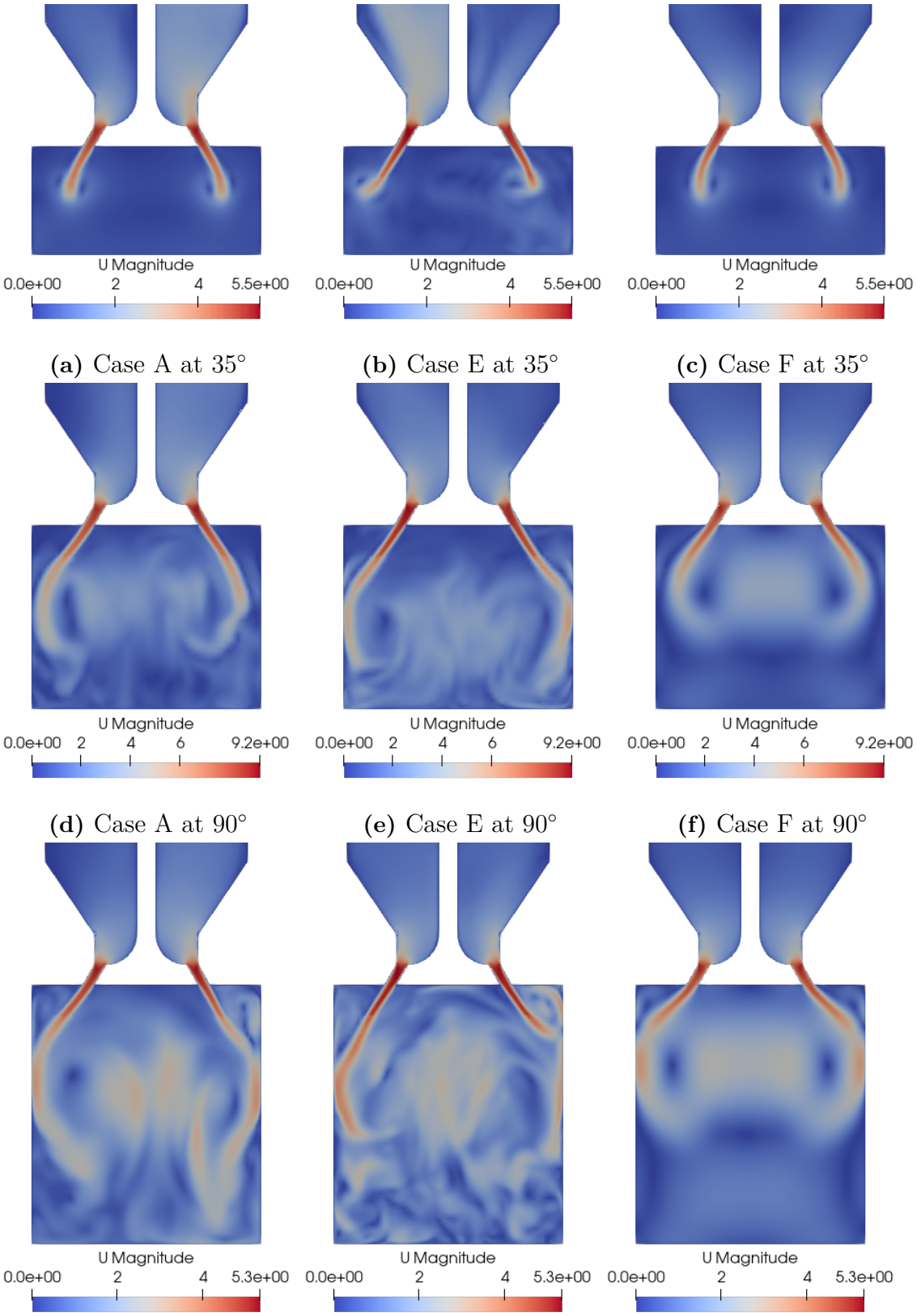

(a) Case A at 35° **(b)** Case E at 35° **(c)** Case F at 35°

(d) Case A at 90° **(e)** Case E at 90° **(f)** Case F at 90°

(g) Case A at 145° **(h)** Case E at 145° **(i)** Case F at 145°

Figure 5.6: Instantaneous velocity magnitude fields for cases of the first study that are using RNG $k-\varepsilon$ (A), $k-\omega$ SST SAS (E) and standard $k-\varepsilon$ (F) turbulence models, at crank angles 35°, 90° and 145° of the third cycle.

the RNG $k-\varepsilon$ and $k-\omega$ SST SAS models have compared to the standard $k-\varepsilon$ model, which provides an explanation for the difference in the amount of resolved TKE.

It is also visible, that the inflow jets have significant variation between their shapes and the jet direction was suspected of in turn having a significant impact on the MAE results for the averaged axial velocity. Of these cases, A had the best agreement to the DNS results with respect to both axial velocity and TKE. It is, however, difficult to visually assess which elements in the field would lead to better agreement with the DNS results as the flow field and the jet are actually fully three-dimensional and cycle-to-cycle variances are taken into account.

5.2 Second study

The MAEs calculated for each case based on the post-processed results are presented in figure 5.7a for the averaged axial velocity and in figure 5.7b for the averaged TKE. Some of the simulations crashed and these are blacked out in the figures. The cases with 4 global surface layers and 0.5 relative first layer thickness weren't run, explaining why they are left blank in the figures.

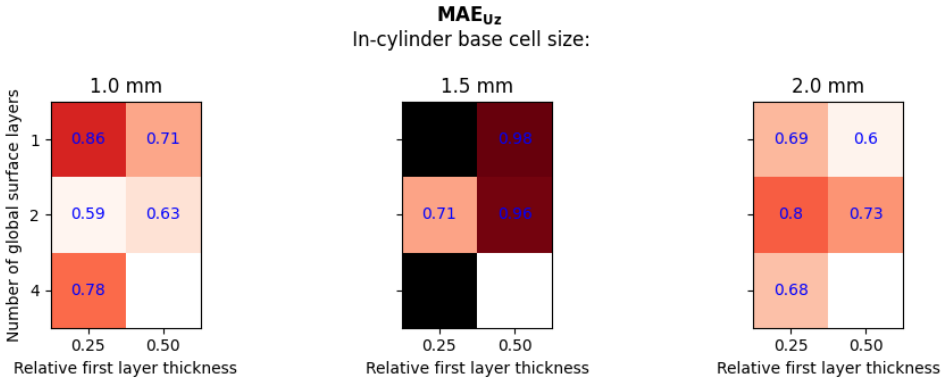

(a) Averaged axial velocity

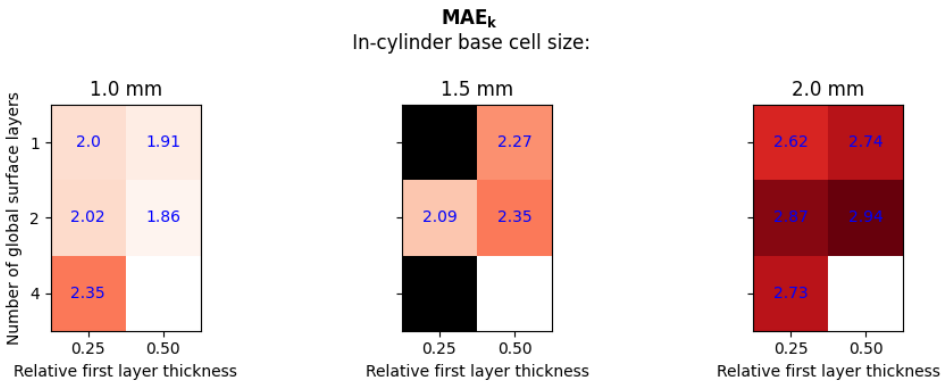

(b) Averaged turbulent kinetic energy

Figure 5.7: MAE values for the second study

Each case had a different mesh and they are presented in figure 5.8. From there it is visible that the inflation layers created by the mesh construction aren't completely consistent with regards to the input parameters. This is especially apparent with the 2.0 mm in-cylinder base cell size cases with a larger number of inflation layers, such as in figure 5.8o, where the inflation layers on the outer rim of the valve port gap have a very variable number of inflation layers.

It mostly seems that the increase in all parameters, cell size, number of inflation layers and the relative thickness of the first layer, negatively affects mesh quality. However, an inconsistency in this statement would be for example the layers at the corner where the inner rim of the valve port gap and the cylinder chamber meet, where there is variation on whether the layers are connected over the corner or not. The latter behavior is present in the cases with one global inflation layer and 0.25 relative first layer thickness, as seen in figures 5.8a, 5.8b and 5.8c, and in the cases with four global inflation layers, 0.50 relative first layer thickness and in-cylinder base cell sizes 1.5 mm and 2.0 mm, as seen in figures 5.8n, 5.8o.

Like in the first study, the 1.5 mm in-cylinder base cell size cases performed again quite poorly, having two crashes and poor results for the averaged axial velocity MAE, as seen in figure 5.7a. This phenomenon has to be somehow linked to the mesh resolution, but visually inspecting the relevant meshes does not reveal any anomalies that could directly explain the exceptionally poor performance, when compared to the 1.0 mm and 2.0 mm in-cylinder base cell size meshes.

From figure 5.7a it can be seen that of the in-cylinder base cell sizes, 1.0 mm and 2.0 mm performed quite similarly with regards to the averaged axial velocity prediction. For 1.0 mm in-cylinder base cell size, the prediction was best with 2 global inflation layers and for 2.0 mm in-cylinder base cell size, the best prediction was with 1 global inflation layer. The theoretical total thicknesses of inflation layers that do not take into account the possible irregularities in the layering have been calculated for table 5.1. There, it can be seen that the aforementioned best predictors of averaged axial velocity are very close in their total inflation layer thicknesses for the respective relative first layer thicknesses. Looking at figure 5.7a, it is not immediately apparent which relative first layer thickness is overall superior.

		In-cylinder base cell size					
		1.0 mm		**1.5 mm**		**2.0 mm**	
Number of global surface layers	**1**	0.1250	0.2500	0.1875	0.3750	0.2500	0.5000
	2	0.2750	0.5500	0.4125	0.8250	0.5500	1.1000
	4	0.6710		1.0065		1.3420	
		0.25	**0.50**	**0.25**	**0.50**	**0.25**	**0.50**
		Relative first layer thickness					

Table 5.1: The theoretical total thickness of the global inflation layers for all cases of the second study (mm).

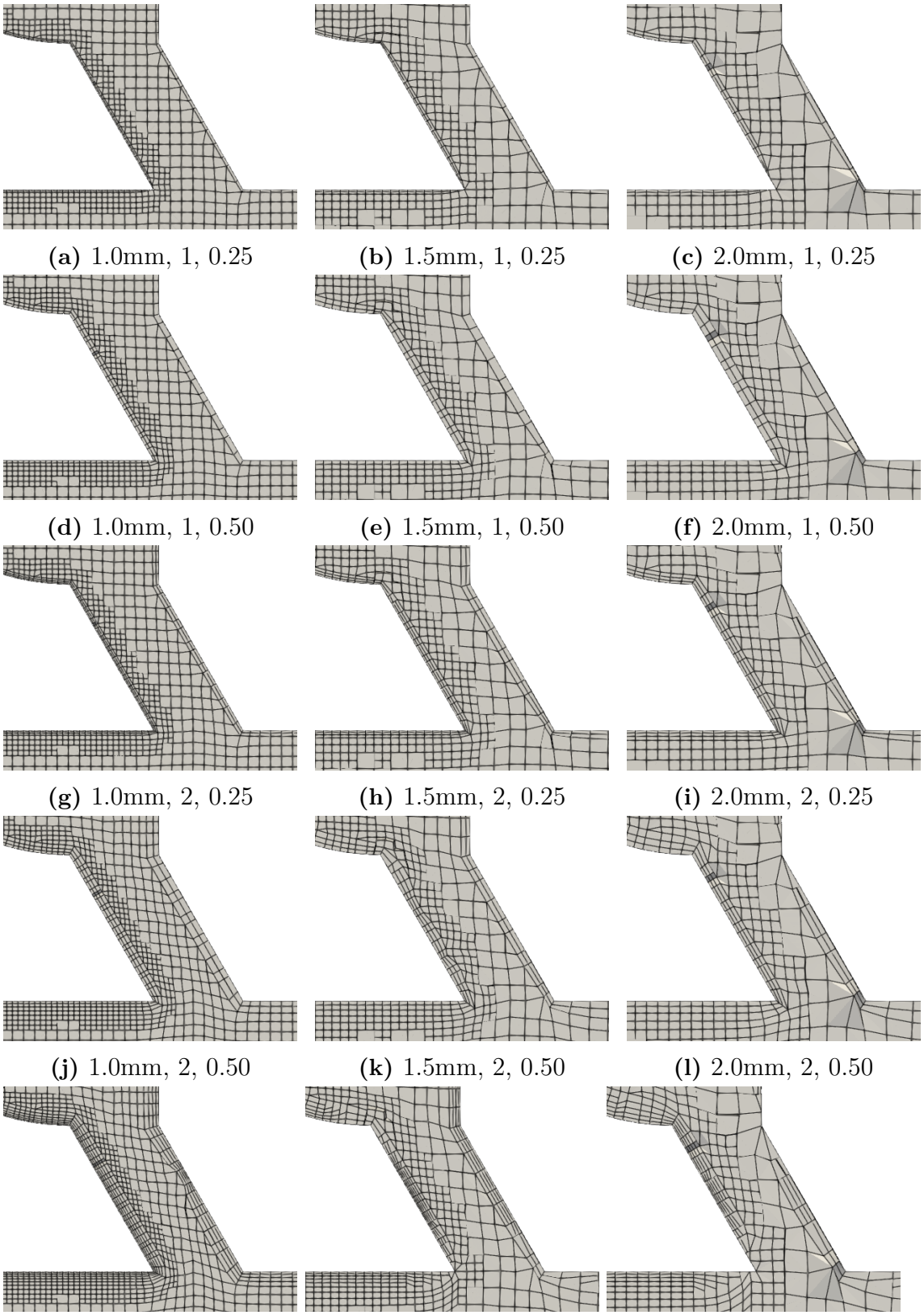

(a) 1.0mm, 1, 0.25 **(b)** 1.5mm, 1, 0.25 **(c)** 2.0mm, 1, 0.25

(d) 1.0mm, 1, 0.50 **(e)** 1.5mm, 1, 0.50 **(f)** 2.0mm, 1, 0.50

(g) 1.0mm, 2, 0.25 **(h)** 1.5mm, 2, 0.25 **(i)** 2.0mm, 2, 0.25

(j) 1.0mm, 2, 0.50 **(k)** 1.5mm, 2, 0.50 **(l)** 2.0mm, 2, 0.50

(m) 1.0mm, 4, 0.25 **(n)** 1.5mm, 4, 0.25 **(o)** 2.0mm, 4, 0.25

Figure 5.8: Mesh cross-section details of the valve port gaps of the cases from the second study. Captions include the in-cylinder base cell size, number of global surface layers and relative first layer thickness, in that order.

Again, like in the first study, the averaged TKE prediction worsens with decreasing mesh resolution, as can be seen in figure 5.7b. This is to be expected. For 1.0 mm in-cylinder base cell size, 1 and 2 global surface layers are superior to 4, and for 2.0 mm in-cylinder base cell size, 1 and 4 layers is slightly superior to 2. Relative first layer thickness of 0.5 seems to be better for the 1.0 mm in-cylinder base cell size cases, and 0.25 for the 2.0 mm cases.

5.3 Third study

The mesh options used in the third study are the same as for one of the meshes of the second study, and a detail of that mesh is presented in figure 5.8j. The calculated MAEs for each case based on the post-processed results are presented in figure 5.9a for the averaged axial velocity and in figure 5.9b for averaged TKE. There are

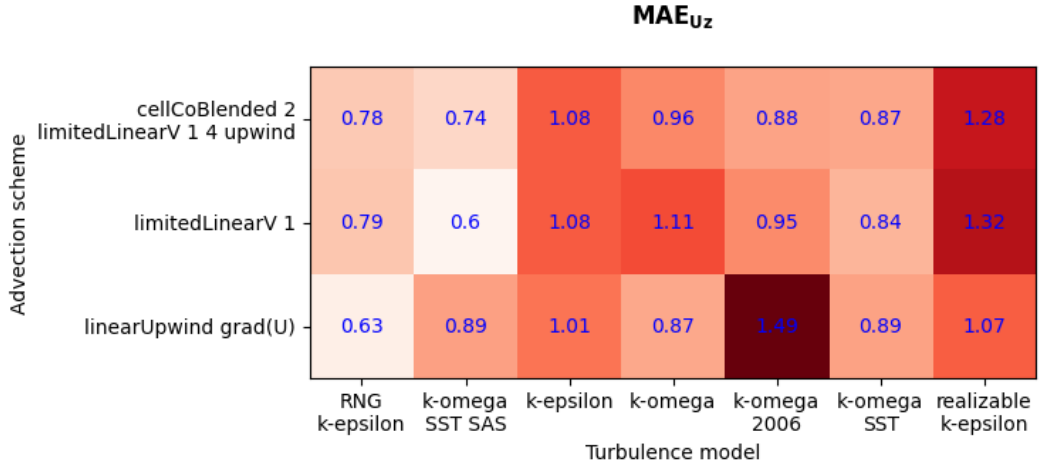

(a) Averaged axial velocity

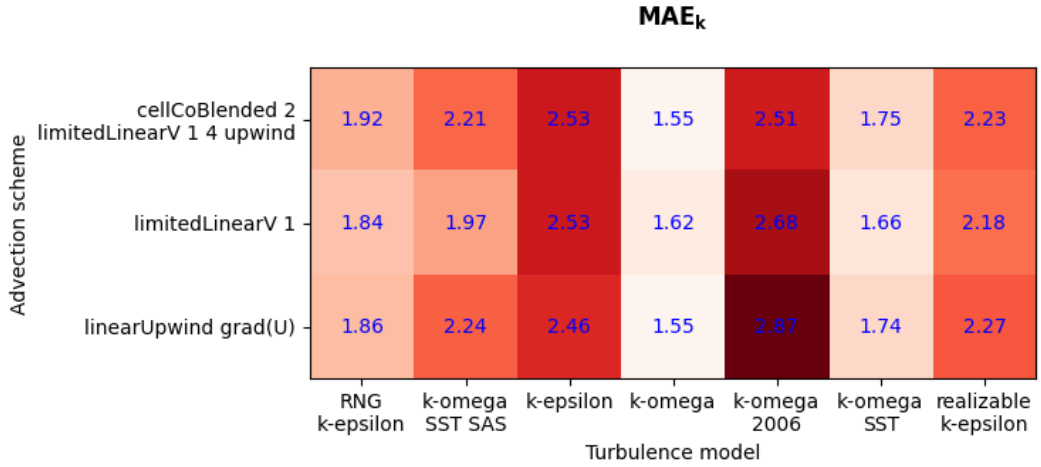

(b) Averaged turbulent kinetic energy

Figure 5.9: MAE values for the third study

some differences in the results between this and the first study for the turbulence

models that were included in both. The only difference between the case setups is the mesh with a different number of layers. While the mesh chosen from the second study showed better performance there, this hasn't directly translated into uniformly better results in this study. For the averaged axial velocity prediction of RNG $k-\varepsilon$ the results are on average slightly worse and for that of $k-\omega$ SST SAS they are on average slightly better, but for both cases the best single result was with the new mesh. For RNG $k-\varepsilon$ it was with `linearUpwind grad(U)` advection scheme and for $k-\omega$ SST SAS it was with `limitedLinearV 1`. For standard $k-\varepsilon$ the averaged axial velocity prediction was improved uniformly, with `linearUpwind grad(U)` advection scheme giving the best result.

For the averaged TKE prediction the differences in the results from the turbulence models also used in the first study were mostly similar to the averaged axial velocity prediction. The only exception being that of the best prediction of averaged TKE with the RNG $k-\varepsilon$ model being with `limitedLinearV 1` advection scheme and the mesh from the first study.

The standout performances from the turbulence models newly introduced in this study are standard $k-\omega$ and $k-\omega$ SST. This is most apparent in their averaged TKE predictions in figure 5.9b as they have performed better than any other turbulence model in this study with all advection schemes. Furthermore, the results for the standard $k-\omega$ model's averaged TKE prediction are the best out of all the studies. In terms of the averaged axial velocity prediction, standard $k-\omega$ had variable results that didn't necessarily stand out from the others and $k-\omega$ SST had fairly good uniform results. The other two newly introduced turbulence models had either poor or very average performance. The $k-\omega$ 2006 model in combination with the `linearUpwind grad(U)` advection scheme had the poorest results for both averaged axial velocity and TKE by a fair margin, and only a little better TKE prediction with the other advection schemes. The realizable $k-\varepsilon$ model had poor results for averaged axial velocity prediction.

For the different velocity advection schemes, it is difficult to notice clear trends in their results. The change in the advection scheme had less of an impact on the averaged TKE prediction than for the averaged axial velocity prediction. The `linearUpwind grad(U)` scheme has the largest variation among its results, mostly due to the exceptionally poor results with $k-\omega$ 2006.

Similarly to the first study, examples of the averaged axial velocity and TKE profiles from the good and poor performers of the cases are inspected.

- For the good case with respect to averaged axial velocity, the case with $k-\omega$ SST SAS turbulence model and `limitedLinearV 1` scheme is chosen, and called case A.
- For the poor case with respect to both averaged axial velocity and TKE, the case with $k-\omega$ 2006 turbulence model and `linearUpwind grad(U)` advection scheme is chosen, and called case B.
- For the good case with respect to averaged TKE, the case with standard

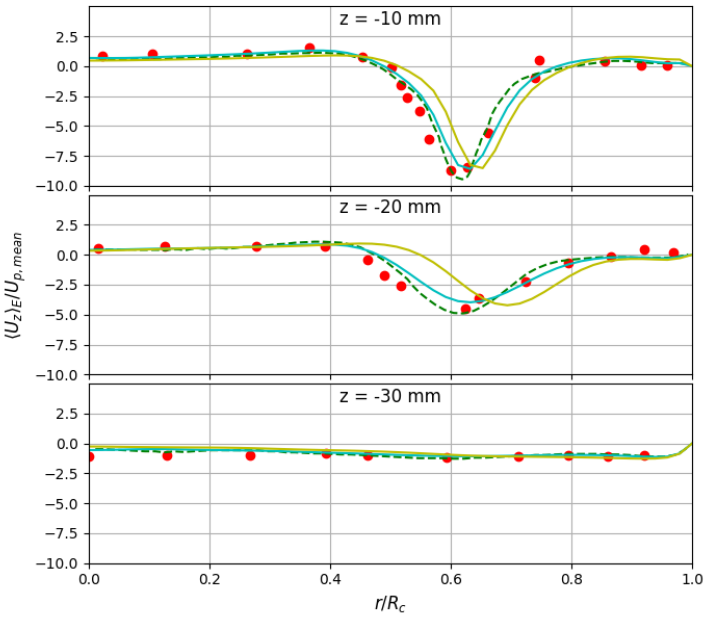

(a) 36°

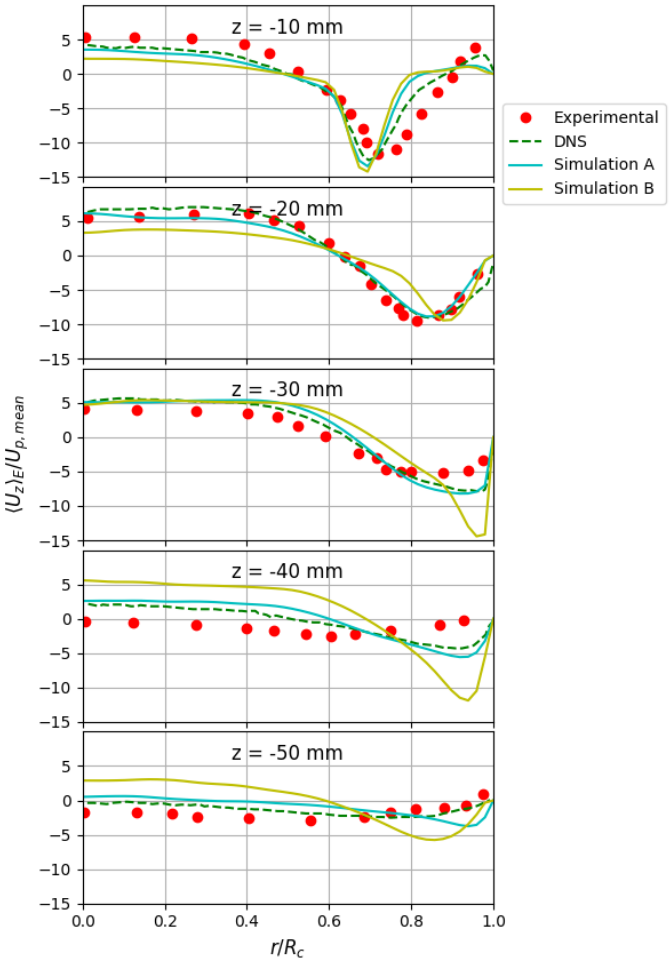

(b) 90°

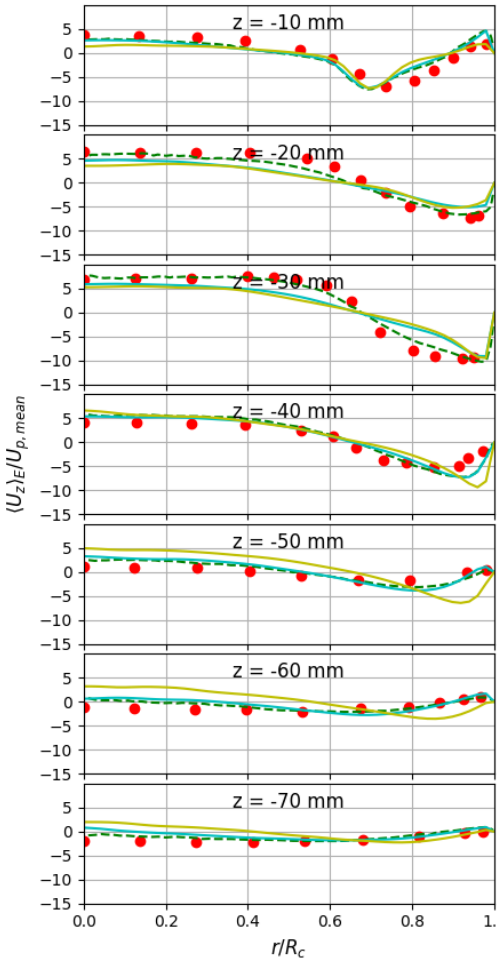

(c) 144°

Figure 5.10: Averaged axial velocity profiles from the third study at specified crank angles for good case A and poor case B, compared against experimental [1] and DNS [17] values.

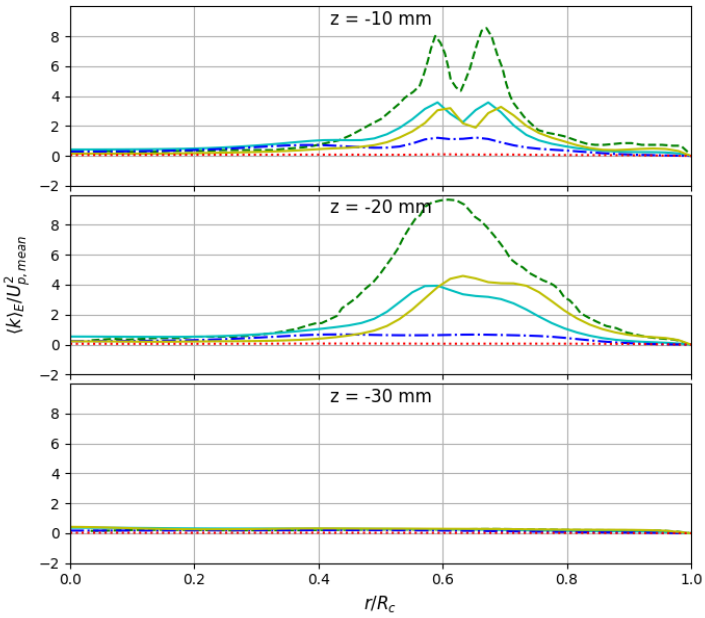

(a) 36°

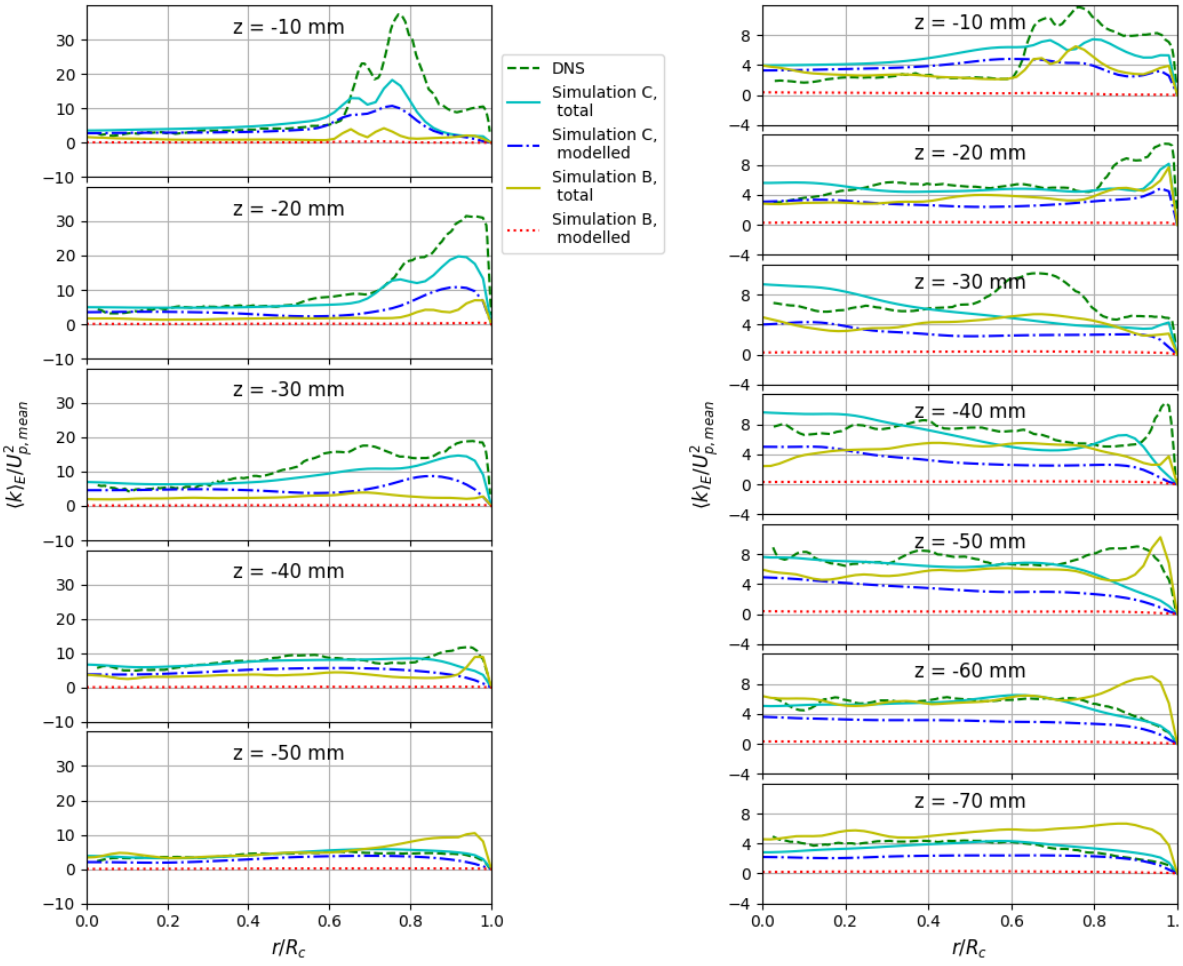

(b) 90°

(c) 144°

Figure 5.11: Averaged total and modelled TKE profiles from the third study at specified crank angles for good case C and poor case B, compared against DNS [17] values.

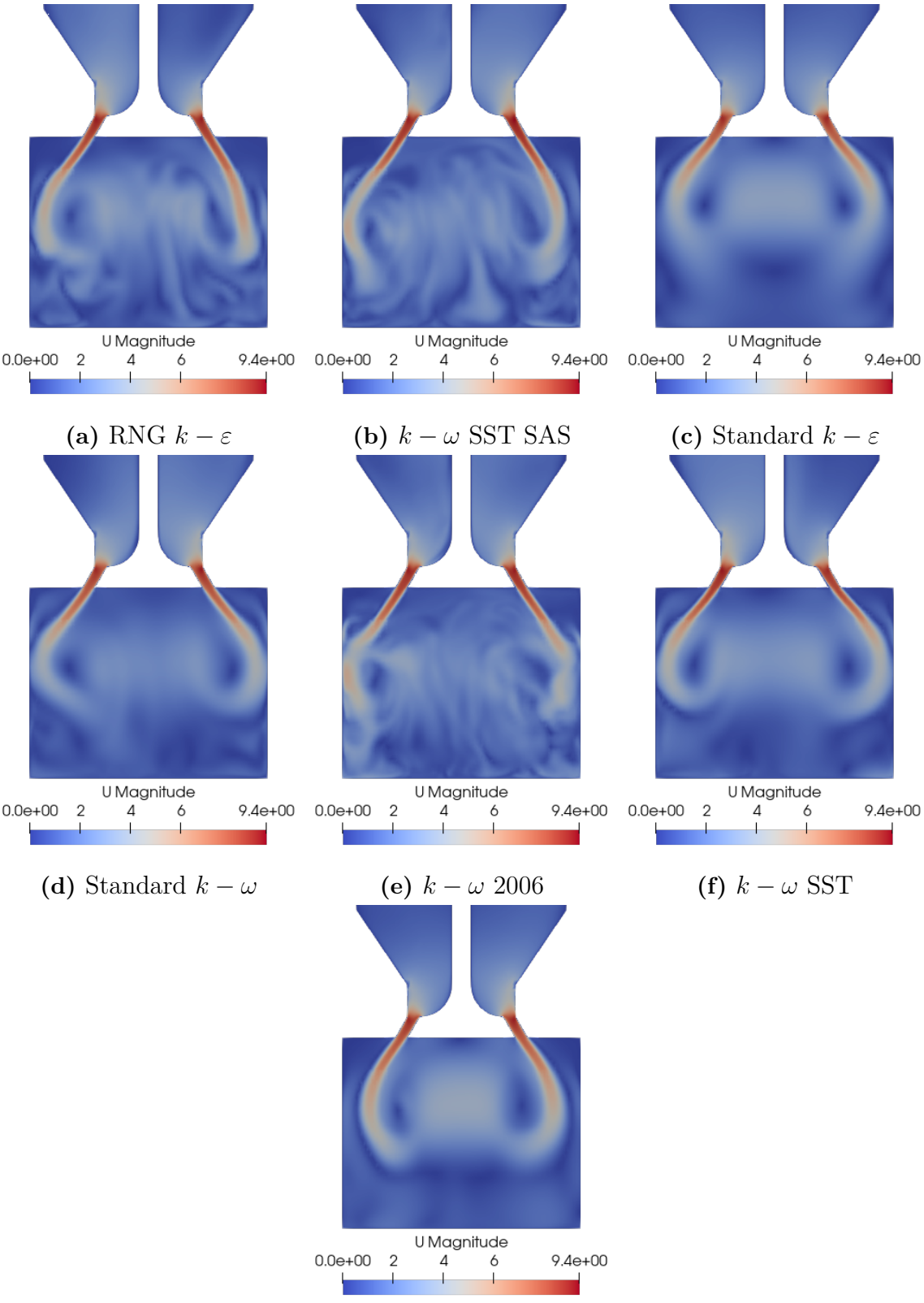

(a) RNG $k-\varepsilon$ **(b)** $k-\omega$ SST SAS **(c)** Standard $k-\varepsilon$

(d) Standard $k-\omega$ **(e)** $k-\omega$ 2006 **(f)** $k-\omega$ SST

(g) Realizable $k-\varepsilon$

Figure 5.12: Instantaneous velocity magnitude fields for cases of the third study that are using `cellCoBlended 2 limitedLinearV 1 4 upwind` and different turbulence models at crank angle 90° of the third cycle.

$k-\omega$ turbulence model and `cellCoBlended 2 limitedLinearV 1 4 upwind` advection scheme is chosen, and called case C.

The averaged axial velocity profiles for different crank angles of cases A and B are presented in figure 5.10. Case B shows a very different kind of deviation from the DNS results than what was observed in the chosen poor case of the first study. Visible especially in figure 5.10b at stations 30 mm and 40 mm below the valve port, the averaged axial velocity profile has a significantly larger peak magnitude than case A or the DNS results, and at stations 40 mm and 50 mm below the valve port and closer to the center of the cylinder the upwards velocity is also larger in magnitude. It seems that in case B the velocity of the jet coming from the valve is overestimated at parts.

The averaged TKE profiles for different crank angles of cases C and B are presented in figure 5.11. Both cases mostly underestimate the magnitude of TKE especially at places where the magnitude predicted by the DNS results is large. Out of the simulations done for this thesis, case C has so far had the best prediction of the averaged TKE when compared to the DNS results. In most parts of figure 5.11 the total TKE profile for case C is close to equal parts modelled and resolved contributions. For case B, the modelled TKE part is almost nonexistent and the resolved TKE is underestimated in most parts, but then greatly overestimated at a few select parts, as can be seen in figure 5.11c at stations 60 mm and 70 mm below the valve port.

The simulated velocity magnitude fields for cases of the third study that all use the `cellCoBlended 2 limitedLinearV 1 4 upwind` advection scheme but different turbulence models are presented in figure 5.12. Turbulence models RNG $k-\varepsilon$, $k-\omega$ SST SAS and standard $k-\varepsilon$ show similar behavior as reported in the first study. Models standard $k-\omega$, $k-\omega$ SST and realizable $k-\varepsilon$ have some unsteady fluctuations in their fields, unlike standard $k-\varepsilon$ but less so than in RNG $k-\varepsilon$ and $k-\omega$ SST SAS. The $k-\omega$ 2006 field has a lot of fluctuations, comparable or even more than in RNG $k-\varepsilon$ and $k-\omega$ SST SAS.

6
Conclusion

In this thesis the performances of different CFD simulation models and parameters were compared when applied to an engine model based on the Imperial college experiment [1]. The engine model had been created in Wärtsilä to be run with the OpenFOAM CFD simulation software, and the modelling choices originally made for it acted as the initial conditions for the model and parameter comparison study. A code was written for the thesis that systematically creates simulation cases based on all the combinations of model and parameter options that the user wants to have be part of the study. The cases are then run with OpenFOAM and after that the simulation results are post-processed with another custom code. Two metrics are calculated for each simulation case that represent the error between their results and a high-fidelity DNS simulation that has been validated against the original experimental results with good agreement [17]. The metrics were calculated from averaged axial velocity and TKE results. These metrics act as qualitative measures of the performance of the respective cases. The performance of the different simulation models and parameters is compared against each other by directly comparing the metrics from cases that use the respective models and parameters, and with other data available from the simulations.

The simulation models and parameters that were considered in three separate comparison studies were turbulence models, velocity advection schemes, values of maximum allowed Courant number, mesh resolution, and the number and thickness of surface inflation layers of the mesh. The performance of the cases in predicting both averaged axial velocity and TKE didn't always coincide. Poor prediction of averaged axial velocity often was due to difference in the direction or magnitude of the inflow jet coming out of the valve port compared to the DNS results. Poor prediction in averaged TKE was often due to great underestimation of the magnitude of TKE, especially at places where the jet was the strongest.

Of the included turbulence models, RNG $k-\varepsilon$, $k-\omega$ SST SAS, standard $k-\omega$ and $k-\omega$ SST performed the best, with the former two more accurate with the averaged axial velocity prediction, and the latter two more accurate with the averaged TKE prediction. The velocity advection schemes did not show major differences in their performance, apart from `linearUpwind grad(U)` performing better with coarser meshes than the other two. Differences in the maximum Courant number had very little effect on performance, with the exception of the maximum Courant number of 10 having more stability issues. Lowering the maximum Courant number from 4 to 1 significantly lengthened the simulation time without improving perfor-

mance. Improving the mesh resolution positively affected averaged TKE prediction performance quite uniformly and vice versa. This was in most parts true for the averaged axial velocity prediction too, with the exclusion of the $k - \varepsilon$ turbulence model, for which the opposite was true. With a specific mesh resolution, where the in-cylinder base cell size was 1.5 mm, there was uncharacteristically poor performance and stability issues. and thickness of surface inflation layers of the mesh had a minor effect on perfomance. The number of surface inflation layers of 1 or 2 gave the best results, depending on the overall mesh resolution and there was no absolute better choice out of the relative first layer thicknesses of 0.25 and 0.50.

6.1 Reflection and recommendations for future work

The objective of this thesis was to investigate the performance differences of different modelling options and parameters for an engine case, and this was accomplished for the Imperial college case. However, the models and parameters that were covered here are only a fraction of all the models and parameters that can go even into a simplified engine model, such as here. Of course, due to limited time and resources, not every option can be considered. The model and parameter choices here were done mostly based on educated guesses on what could have an impact on the performance and by choosing models and parameters where previously the choices for similar cases had been ambiguous. There was no clear methodology for finding out which models and parameters would be most worth studying in order to have the most impact on the model performance.

It is also relevant to question what is the benefit of performing these studies for a single engine model, which furthermore lacks many of the properties that conventional engines have, such as opening and closing valves, or combustion. There is a high chance that the variety seen in the results when using different models and parameters is at some level tied to the specifics of this model and the initial choices that have been made when the model has been created and were not changed in the studies done here. If the results could be shown to be somewhat replicable for other engine models, the value of the findings would be arguably much greater, as they could infer for possible generalizability of the studies.

The performance comparison metric used in this thesis was effective for the comparison of the performance differences between a large number of cases using different models and parameters. For future work, more of the comparison studies that were carried out here could be performed, but perhaps more thought has to be put into the parameters and models of choice that being compared. Design of experiment (DOE) methods could be used to refine the model and parameter combination matrices, so that more options could be chosen without having to run a very large amount of cases. An other way to continue would be to apply the methodology presented in the thesis on one or a few other engine models, like the TCC-III engine [2] or the TU Darmstadt engine [3].

Bibliography

[1] A. P. Morse, J. H. Whitelaw, and M. Yianneskis, "Turbulent flow measurements by laser-doppler anemometry in motored piston-cylinder assemblies," *Journal of Fluids Engineering*, vol. 101, pp. 208–216, 1979.

[2] I. Ko, F. Rulli, S. Fontanesi, A. d'Adamo, and K. Min, "Methodology for the large-eddy simulation and particle image velocimetry analysis of large-scale flow structures on tcc-iii engine under motored condition," *International Journal of Engine Research*, vol. 22, no. 8, pp. 2709–2731, 2021. DOI: 10.1177/1468087420934599. eprint: https://doi.org/10.1177/1468087420934599. [Online]. Available: https://doi.org/10.1177/1468087420934599.

[3] I. Clara, B. Fabio, B. Alessio, and F. Stefano, "A preliminary 1d-3d analysis of the darmstadt research engine under motored condition," *E3S Web Conf.*, vol. 197, p. 06 006, 2020. DOI: 10.1051/e3sconf/202019706006. [Online]. Available: https://doi.org/10.1051/e3sconf/202019706006.

[4] C. Hirsch, *Numerical computation of internal and external flows. Volume 1, Fundamentals of computational fluid dynamics*, 2nd ed. Elsevier, 2007, ISBN: 978-0-7506-6594-0. [Online]. Available: https://app.knovel.com/hotlink/toc/id:kpNCIEFFC2/numerical-computation/numerical-computation.

[5] O. Zikanov, *Essential Computational Fluid Dynamics*. John Wiley Sons, Incorporated, 2010. [Online]. Available: https://ebookcentral.proquest.com/lib/aalto-ebooks/detail.action?docID=819001.

[6] C. J. Greenshields and H. G. Weller, *Notes on Computational Fluid Dynamics: General Principles*. Reading, UK: CFD Direct Ltd, 2022.

[7] S. B. Pope, *Turbulent Flows*. Cambridge University Press, 2000.

[8] B. E. Launder and B. I. Sharma, "Application of the energy-dissipation model of turbulence to the calculation of flow near a spinning disc," *Letters in Heat and Mass Transfer*, vol. 1, no. 2, pp. 131–137, 1974.

[9] W. L. Oberkampf and T. G. Trucano, "Verification and validation in computational fluid dynamics," *Progress in Aerospace Sciences*, vol. 38, no. 3, pp. 209–272, 2002, ISSN: 0376-0421. DOI: https://doi.org/10.1016/S0376-0421(02)00005-2. [Online]. Available: https://www.sciencedirect.com/science/article/pii/S0376042102000052.

[10] R. De Robbio, M. C. Cameretti, E. Mancaruso, R. Tuccillo, and B. M. Vaglieco, "Cfd study and experimental validation of a dual fuel engine: Effect of engine speed," *Energies*, vol. 14, no. 14, 2021, ISSN: 1996-1073. DOI: 10.3390/en14144307. [Online]. Available: https://www.mdpi.com/1996-1073/14/14/4307.

[11] J. E. Bardina, P. G. Huang, and T. J. Coakley, "Turbulence modeling validation, testing, and development," *NASA Technical Memorandum*, vol. 110446, pp. 10–2514, 1997.

[12] *Ercoftac "classic collection" database*, http://cfd.mace.manchester.ac.uk/ercoftac/doku.php?id=start, Accessed: 2025-10-27.

[13] *Nasa langley research center, turbulence modeling resource*, https://turbmodels.larc.nasa.gov/index.html, Accessed: 2025-10-27.

[14] Y. Li, E. Perlman, M. Wan, *et al.*, "A public turbulence database cluster and applications to study lagrangian evolution of velocity increments in turbulence," *Journal of Turbulence 9*, no. 31, 2008.

[15] *Kth stockholm, turbulence data from philipp schlatter*, https://www.mech.kth.se/~pschlatt/DATA/, Accessed: 2025-10-27.

[16] J. Oldengarm, "Development of rotating diffraction gratings and their use in laser anemometry," *Optics Laser Technology*, vol. 9, no. 2, pp. 69–71, 1977.

[17] M. Schmitt, C. E. Frouzakis, A. G. Tomboulides, Y. M. Wright, and K. Boulouchos, "Direct numerical simulation of multiple cycles in a valve/piston assembly," *Physics of Fluids*, vol. 26, no. 3, 2014.

[18] A. Montorfano, F. Piscaglia, and A. Onorati, "A les study on the evolution of turbulent structures in moving engine geometries by an open-source cfd code," *SAE TECHNICAL PAPER*, vol. 1, pp. 1–15, 2014.

[19] C. Speziale and S. Thangam, "Analysis of an rng based turbulence model for separated flows," *International Journal of Engineering Science*, vol. 30, no. 10, 1379–IN4, 1992, ISSN: 0020-7225. DOI: https://doi.org/10.1016/0020-7225(92)90148-A. [Online]. Available: https://www.sciencedirect.com/science/article/pii/002072259290148A.

DEPARTMENT OF SOME SUBJECT OR TECHNOLOGY
CHALMERS UNIVERSITY OF TECHNOLOGY
Gothenburg, Sweden
www.chalmers.se

CHALMERS
UNIVERSITY OF TECHNOLOGY